Angewandte Chemie
Eine Zeitschrift der Gesellschaft Deutscher Chemiker

Supporting Information

Template-Directed Synthesis of Strained *meso-meso*-Linked Porphyrin Nanorings

J. M. Van Raden, J.-R. Deng, H. Gotfredsen, J. Hergenhahn, M. Clarke, M. Edmondson, J. Hart, J. N. O'Shea, F. Duarte, A. Saywell, H. L. Anderson**

SUPPORTING INFORMATION

Supporting Information

69451 Weinheim, Germany

Template-Directed Synthesis of Strained *meso-meso*-Linked Porphyrin Nanorings

Jeff M. Van Raden[+],[a] Jie-Ren Deng[+],[a] Henrik Gotfredsen[+],[a] Janko Hergenhahn,[a] Michael Clarke,[a] Matthew Edmondson,[a] Jack Hart,[a] James N. O'Shea,[a] Fernanda Duarte,[a] Alex Saywell,*[b] and Harry L. Anderson*[a]

Abstract: Strained macrocycles display interesting properties, such as conformational rigidity, often resulting in enhance π-conjugation or enhanced affinity for non-covalent guest binding, yet they can be difficult to synthesize. Here we use computational modeling to design a template to direct the formation of an 18-porphyrin nanoring with direct *meso-meso* bonds between the porphyrin units. Coupling of a linear 18-porphyrin oligomer in the presence of this template gives the target nanoring, together with an unexpected 36-porphyrin ring by-product. Scanning tunneling microscopy (STM) revealed the elliptical conformations and flexibility of these nanorings on a Au(111) surface.

DOI: 10.1002/anie.2021XXXXX

SUPPORTING INFORMATION

Table of Contents

Section S1 General Remarks S2
Section S2 Overview of Synthesis S3
Section S3 Synthetic Procedures and Compound Characterization S4
Section S4 UV–Visible Titrations S11
Section S5 Computational Modeling S14
Section S6 Scanning Tunnelling Microscopy S21
Section S7 NMR, Mass, UV–vis–NIR Absorption and Fluorescence Spectra S24
Section S8 References S43
Author Contributions S43

S1 General Remarks

All reagents (Acros, Aldrich, Fluorochem, and TCI) were purchased as reagent grade and used without further purification. Solvents for extraction or column chromatography were used in HPLC grade. Dry solvents for reactions were purified by the solvent drying system MBraun MB-SPS-5-Bench Top under nitrogen atmosphere (H_2O content < 20 ppm as determined by Karl Fischer titration). Flash column chromatography was performed using SiO_2 (60 Å, 230−400 mesh, particle size 0.040−0.063 mm, Merck) at 25 °C. Analytical thin layer chromatography (TLC) was performed on aluminum sheets coated with silica gel 60 F254 (Merck). Visualization was achieved using UV light (254 or 365 nm). Size exclusion chromatography (SEC) was carried out using Bio-Beads S-X1.

NMR data were recorded at 400 MHz using a Bruker AVII400 or AVIII400, at 500 MHz using a Bruker AVII500 (with DUAL cryoprobe) or DRX500, or at 600 MHz using a Bruker AVIII 600 (with broadband cryo-probe), or at 700 MHz using a Bruker AVIII700 (with TCI cryoprobe). Chemical shifts are quoted as parts per million (ppm) relative to residual $CHCl_3$ (δ_H 7.26 ppm for ^1H NMR and at δ_C 77.2 ppm for ^{13}C NMR). Multiplicity (s = singlet, d = doublet, t = triplet, q = quartet, m = multiplet) and coupling constants were reported whenever possible. ^1H NMR signals were assigned based on comparison between compounds, chemical shifts, integrals and coupling constants.

MALDI-TOF spectra were measured using a Bruker MicroflexTM LRF and DCTB matrix.

UV–vis–NIR absorbance measurements were recorded at 298 K with a Perkin-Elmer Lambda 20 photospectrometer using quartz 1 cm cuvettes and temperature was controlled by a PTP-1 peltier unit from Perkin Elmer. Fluorescence spectra were acquired using an Edinburgh Instruments FS5 spectrofluorometer operating Fluoracle® software, equipped with a xenon arc lamp (providing 230–1000 nm excitation range), a thermostatic sample holder (SC-20) and both an R13456 PMT detector (200–950 nm spectral coverage, Hamamatsu) and an InGaAs analogue NIR detector (850–1650 nm spectral coverage).

The compounds hexakis(4-bromophenyl)benzene,[1] 2-bromo-5-chloro-1,3-diiodobenzene,[2] 2-bromo-1,3-bis(octyloxy)benzene,[3] porphyrin monomer **P1**,[4] *meso–meso* linked porphyrin trimer ***l*-P3**,[4,5] octadecamer ***l*-P18**,[5] and porphyrin nanorings ***c*-P24b**[5] were prepared according to published procedures.

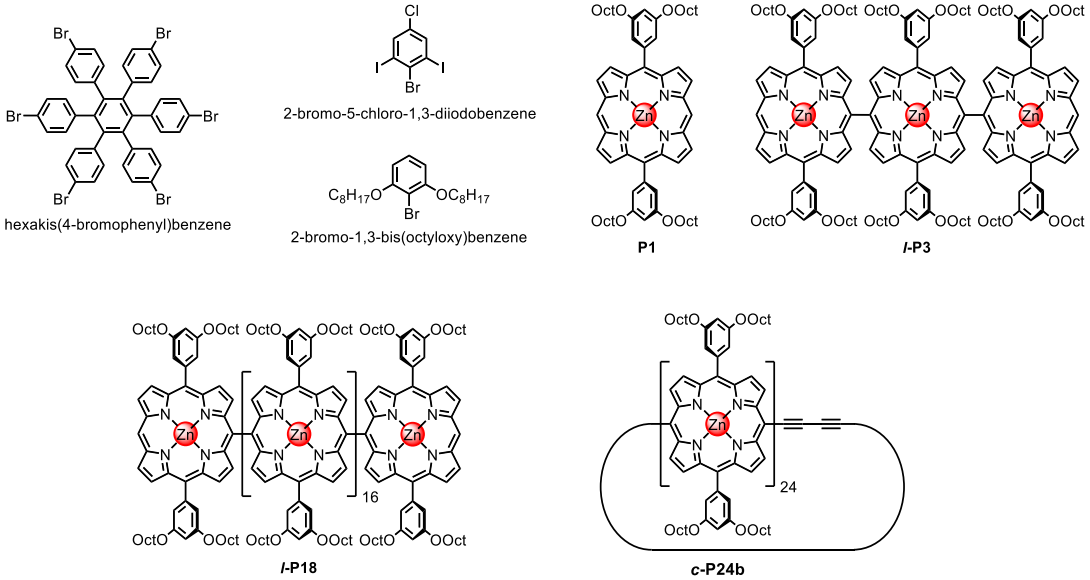

Figure S1. Overview of synthesized known compounds.

SUPPORTING INFORMATION

S2 Overview of Synthesis

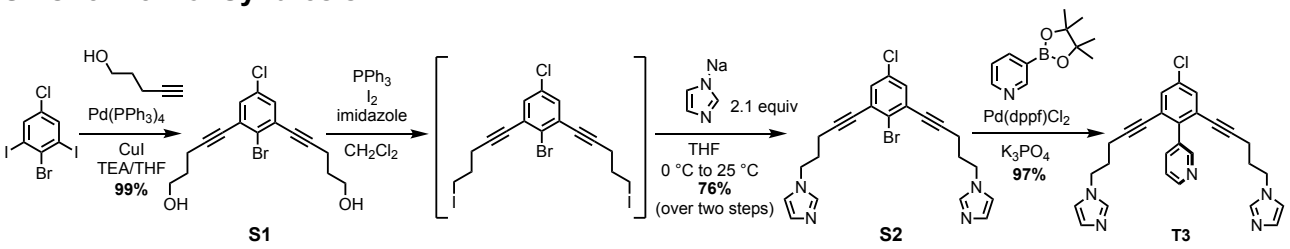

Figure S2. Synthetic route used to access three-legged chloride **T3**.

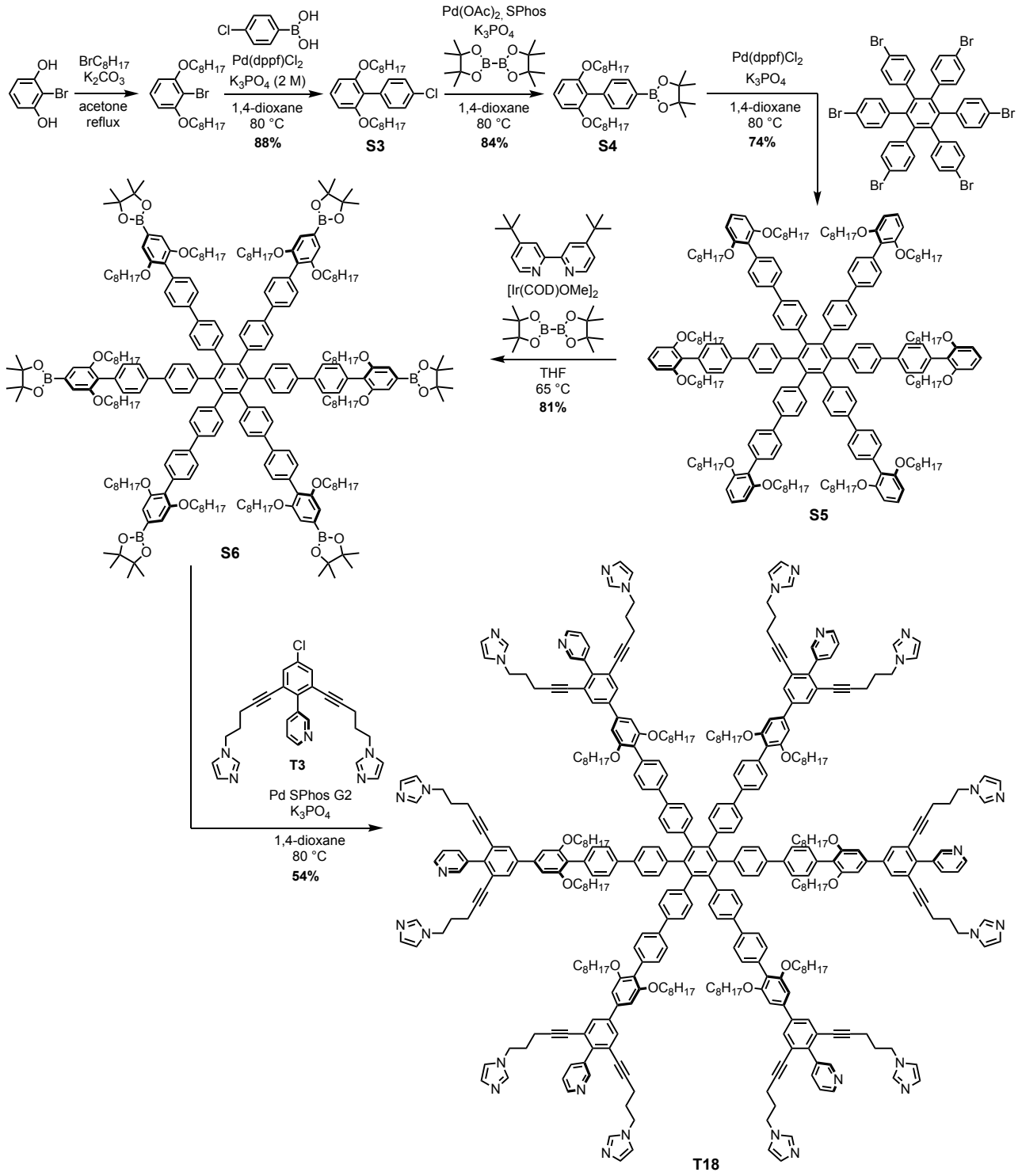

Figure S3. Synthetic route used to access template **T18**.

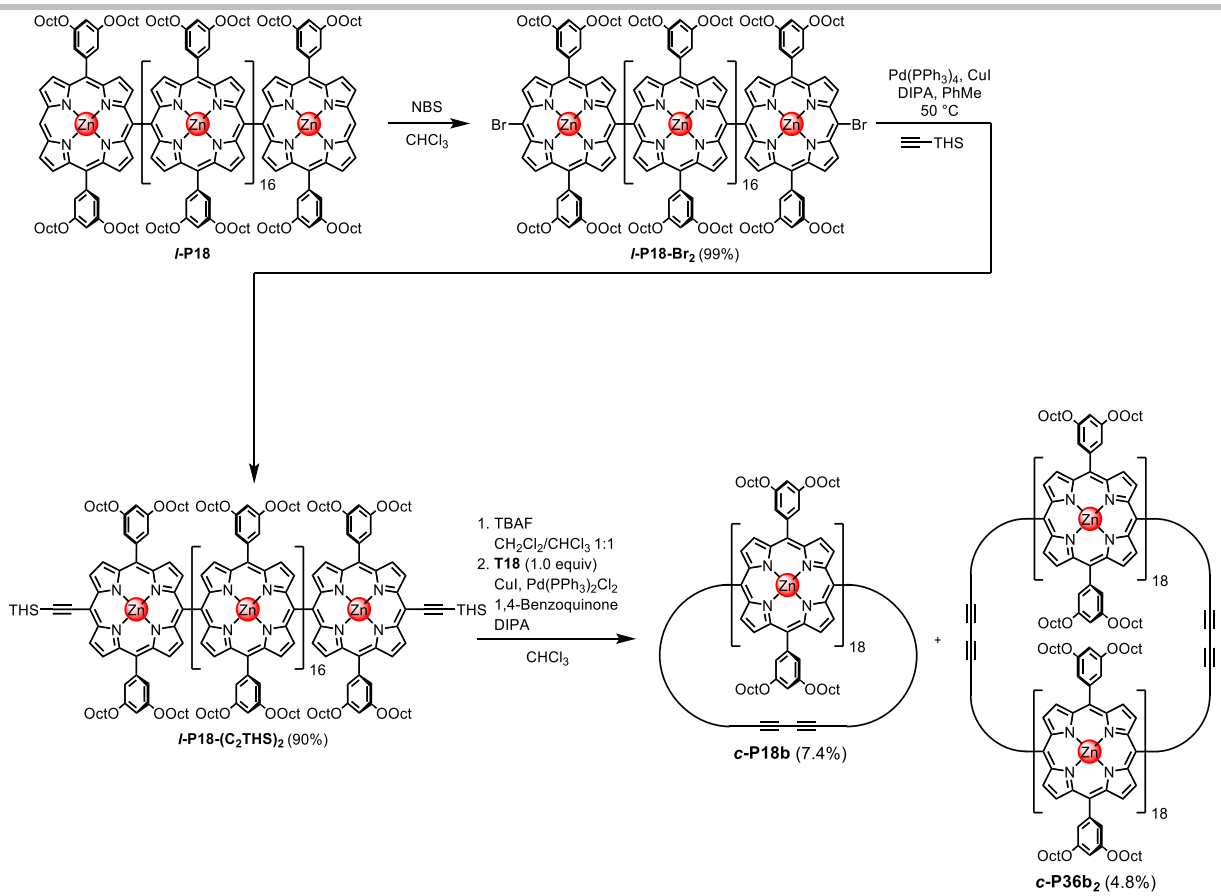

l-P18

l-P18-Br$_2$ (99%)

l-P18-(C$_2$THS)$_2$ (90%)

c-P18b (7.4%)

c-P36b$_2$ (4.8%)

Figure S4. Synthetic route used to access cyclic structures ***c*-P18b** and ***c*-P36b$_2$**.

S3 Synthetic Procedures and Compound Characterization

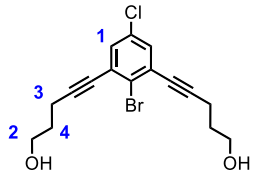

Compound S1. To a Schlenk flask equipped with a stir bar was added 2-bromo-5-chloro-1,3-diiodobenzene (5.8 g, 13 mmol, 1.0 equiv.), CuI (0.25 g, 1.3 mmol, 0.10 equiv.), and Pd(PPh$_3$)$_4$ (0.76 g, 0.66 mmol, 0.05 equiv.). The flask was evacuated and back-filled with N_2 five times. In a separate flask, THF and NEt$_3$ (1:1, 10 mL) were subjected to three freeze-pump-thaw cycles. This solution was then transferred to the Schlenk flask followed by the addition of 4-pentyn-1-ol (2.7 mL, 29 mmol, 2.2 equiv.). The reaction mixture was then stirred overnight then passed through a small bed of celite. The filtrate was collected, concentrated and the resulting dark oil was chromatographed on SiO_2 (30% EtOAc/CH_2Cl_2) to give the desired compound as a slightly yellow oil (4.6 g, 99%).

^{1}H NMR (400 MHz, $CDCl_3$) δ 7.22 (s, 2H, **H$_1$**), 3.81 (t, *J* = 6.1 Hz, 4H, **H$_2$**), 2.56 (t, *J* = 6.9 Hz, 4H, **H$_3$**), 2.00 – 1.80 (m, 4H, **H$_4$**), 1.49 (s, 2H, **H$_{OH}$**).

^{13}C NMR (101 MHz, $CDCl_3$) δ 132.57, 132.03, 127.98, 126.57, 96.21, 79.29, 61.77, 31.17, 16.31.

ESI-HRMS: *m/z* 355.0095 (calculated for $[C_{16}H_{17}O_2ClBr]^+$ = $[M+H]^+$: 355.0095).

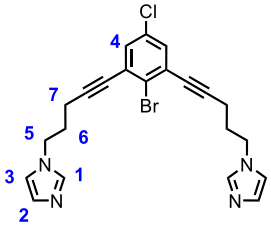

Compound S2. To a flame-dried 100 mL round bottom flask equipped with a stir bar was added PPh_3 (7.5 g, 29 mmol, 3.0 equiv.) and I_2 (7.3 g, 29 mmol, 3.0 equiv.) followed by CH_2Cl_2 (50 mL). The contents were allowed to stir for 10 minutes and the solution turned bright orange. As a solid, imidazole (3.3 g, 48 mmol, 5.0 equiv.) was then added which resulted in the formation of white precipitate. After stirring for an additional 10 minutes, **S1** (3.4 g, 9.6 mmol, 1.0 equiv.) was then quickly added (as solution in 5.0 mL CH_2Cl_2) and the reaction was monitored until all starting material was consumed (typically 1 h). The reaction was then quenched by adding an aqueous $Na_2S_2O_3$ solution (25 mL, 1.0 M) and then transferred to a separatory funnel. The organic phase was then washed with H_2O (3 x 25 mL), followed by brine (1 x 25 mL), and then dried over sodium sulfate. After removal of the solvent via rotary evaporation, the resulting yellow/brown solid

was passed through a pad of silica (5% EtOAc/PE) which, after removal of solvent, gave an orange oil (5.5 g, 100%). This orange oil was then used directly in the next step and scaled as needed.

To a flame-dried 100 mL round bottom flask equipped with a stir bar was added imidazole (0.31 g, 4.6 mmol, 2.1 equiv.) and THF (25 mL). This solution was then cooled to 0 °C and NaH (0.12 g, 4.8 mmol, 2.2 equiv.) was added resulting in a white suspension. After stirring 10 minutes, the reaction was allowed to warm to room temperature and a portion of the above mentioned orange oil (0.77 g, 2.2 mmol, 1.0 equiv.) was added (as a solution in 5 mL THF). The contents were stirred overnight and the progress was monitored via TLC. On completion, the reaction was quenched with MeOH (1.0 mL) and the solvent was removed to give an orange oil which, after chromatography (SiO_2 5% MeOH/$CHCl_3$), gave the desired compound as a tan crystalline solid (0.75 g, 76% over two steps).

^{1}H NMR (400 MHz, $CDCl_3$) δ 7.57 (s, 2H, **H_1**), 7.34 (s, 2H, **H_4**), 7.08 (s, 2H, **H_2**), 6.97 (s, 2H, **H_3**), 4.21 (t, *J* = 6.7 Hz, 4H, **H_5**), 2.45 (t, *J* = 6.6 Hz, 4H, **H_7**), 2.08 (quint, *J* = 6.7 Hz, 4H, **H_6**).

^{13}C NMR (101 MHz, $CDCl_3$) δ 137.47, 132.88, 132.35, 129.79, 127.66, 126.66, 119.01, 94.54, 80.26, 45.42, 29.63, 16.69.

ESI-HRMS: *m/z* 455.0630 (calculated for $[C_{22}H_{21}N_4ClBr]^+$ = $[M+H]^+$: 455.0633).

Compound T3. To a 100 mL round bottom flask equipped with a stir bar was added **S2** (0.47 g, 1.0 mmol, 1.0 equiv.), 3-pyridineboronic acid pinacol ester (0.21 g, 1.0 mmol, 1.0 equiv.), and Pd(dppf)Cl_2 (0.15 g, 0.21 mmol, 0.2 equiv.). The flask was evacuated and back-filled with N_2 five times, followed by addition of 1,4-dioxane (20 mL). This solution was then vigorously sparged with N_2 for 1 h, and it was then placed into an oil bath at 80 °C. A N_2 sparged aqueous solution of K_3PO_4 (2.0 mL, 2 M, 4.0 mmol, 4.0 equiv.) was added, quickly turning the solution to a dark orange. The reaction was stirred overnight. The contents were then cooled to room temperature and passed through a bed of celite. After removal of the solvent via rotary evaporation, the resulting brown oil was chromatographed (7% MeOH/$CHCl_3$) to give the target compound as a slightly brown oil (0.41 g, 88%).

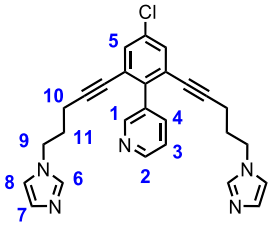

^{1}H NMR (400 MHz, $CDCl_3$) δ 8.68 (d, *J* = 1.4 Hz, 1H, **H_1**), δ 8.60 (d, *J* = 1.1 Hz, 1H, **H_2**), 7.74 (dt, *J* = 7.8, 1.9 Hz, 1H **H_4**), 7.43 (s, 2H **H_5**), 7.33 (ddd, *J* = 7.8, 4.9, 0.9 Hz, 1H **H_3**), 7.30 (s, 2H **H_6**), 7.00 (s, 2H, **H_7**), 6.75 (s, 2H, **H_8**), 3.72 (t, *J* = 6.8 Hz, 4H, **H_9**), 2.17 (t, *J* = 6.6 Hz, 4H, **H_{10}**), 1.76 (p, *J* = 6.7 Hz, 4H, **H_{11}**).

^{13}C NMR (101 MHz, $CDCl_3$) δ 150.62, 148.96, 140.64, 137.77, 137.41, 134.92, 133.71, 131.92, 129.78, 125.08, 122.88, 119.31, 93.50, 79.71, 45.19, 29.34, 16.33.

ESI-HRMS: *m/z* 476.1613 (calculated for $[C_{27}H_{24}N_5ClNa]$ = $[M+Na]^+$: 476.1612).

Compound S3. To a 100 mL round bottom flask equipped with a stir bar was added 2-bromo-1,3-bis(octyloxy)benzene (4.5 g, 11 mmol, 1.0 equiv.), 4-chlorophenylboronic acid (2.2 g, 14 mmol, 1.3 equiv.), and Pd(dppf)Cl_2 (0.80 g, 1.1 mmol, 0.1 equiv.). The flask was evacuated and back-filled with N_2 five times, followed by addition of 1,4-dioxane (50 mL). This solution was then vigorously sparged with N_2 for 1 h, and it was then placed into an oil bath at 80 °C. An N_2 sparged aqueous solution of K_3PO_4 (16 mL, 2 M, 33 mmol, 3.0 equiv.) was added, quickly turning the solution to a dark orange. The reaction was stirred overnight. The contents were then cooled to room temperature and passed through a bed of celite. After removal of the solvent via rotary evaporation, the resulting brown oil was chromatographed (30% CH_2Cl_2/PE) to give the target compound as a colorless oil (4.3 g, 88%).

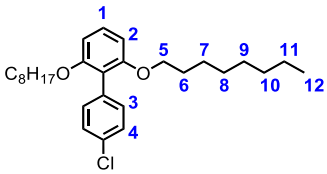

^{1}H NMR (400 MHz, $CDCl_3$) δ 7.39 – 7.27 (m, 4H, **$H_{3,4}$**), 7.22 (t, *J* = 8.3 Hz, 1H, **H_1**), 6.61 (d, *J* = 8.3 Hz, 2H, **H_2**), 3.88 (t, *J* = 6.4 Hz, 4H, **H_5**), 1.87 – 1.56 (m, 4H, **H_6**), 1.32 – 0.76 (m, 26H, **$H_{7–12}$**).

^{13}C NMR (101 MHz, $CDCl_3$) δ 157.80, 132.86, 132.71, 132.19, 128.90, 127.52, 118.31, 105.99, 69.40, 31.90, 29.37, 29.29, 29.24, 26.10, 23.42, 15.22.

ESI-HRMS: *m/z* 445.2869 (calculated for $[C_{28}H_{42}O_2Cl]^+$ = $[M+H]^+$: 445.2868).

Compound S4. To a 100 mL round bottom flask equipped with a stir bar was added **S3** (4.1 g, 9.1 mmol, 1.0 equiv.), K_3PO_4 (5.8 g, 27 mmol, 3.0 equiv.), and Pd(OAc)$_2$ (0.20 g, 1.8 mmol, 0.1 equiv.), SPhos (0.75 g, 1.8 mmol, 0.2 equiv.), and bis(pinacolato)diboron (4.6 g, 18 mmol, 2.0 equiv.). The flask was evacuated and back-filled with N_2 five times, followed by addition of N_2 sparged 1,4-dioxane (50 mL). This solution was then placed into an oil bath at 80 °C and allowed to stir overnight. The contents were then cooled to room temperature and passed through a bed of celite. After removal of the solvent via rotary evaporation, the resulting brown oil was chromatographed (50% CH_2Cl_2/PE) to give the target compound as a colorless oil (4.1 g, 84%)

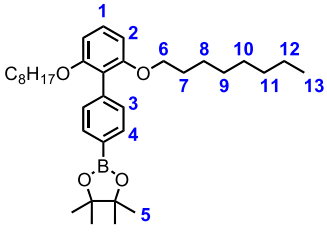

^{1}H NMR (400 MHz, $CDCl_3$) δ 7.80 (d, *J* = 8.1 Hz, 2H, **H_4**), 7.37 (d, *J* = 8.1 Hz, 2H, **H_3**), 7.20 (t, *J* = 8.3 Hz, 1H, **H_1**), 6.61 (d, *J* = 8.3 Hz, 2H, **H_2**), 3.87 (t, *J* = 6.5 Hz, 4H, **H_6**), 1.59 (m, 4H, **H_7**), 1.36 (s, 12H, **H_5**), 1.33 – 0.76 (m, 26H, **$H_{8–13}$**).

^{13}C NMR (101 MHz, $CDCl_3$) δ 157.33, 137.59, 133.79, 130.69, 128.68, 120.52, 105.70, 83.70, 68.87, 31.89, 29.32, 29.28, 29.21, 26.05, 25.06, 22.78, 14.25.

ESI-HRMS: *m*/*z* 537.4116 (calculated for $[C_{34}H_{54}O_4B]^+$ = $[M+H]^+$: 537.4113).

Compound S5. To a 100 mL round bottom flask equipped with a stir bar was added **S4** (0.50 g, 0.94 mmol, 7.0 equiv.), hexakis(4-bromophenyl)benzene (0.14 g, 0.13 mmol, 1.0 equiv.), and $Pd(dppf)Cl_2$ (59 mg, 0.08 mmol, 0.6 equiv.). The flask was evacuated and back-filled with N_2 five times, followed by addition of 1,4-dioxane (50 mL). This solution was then vigorously sparged with N_2 for 1 h, and it was then placed into an oil bath at 80 °C. An N_2 sparged aqueous solution of K_3PO_4 (1.3 mL, 2 M, 2.7 mmol, 20 equiv.) was added, quickly turning the solution to a dark orange. The reaction was stirred overnight. The contents were then cooled to room temperature and passed through a bed of celite. After removal of the solvent via rotary evaporation, the resulting brown oil was chromatographed (30% CH_2Cl_2/PE) to give the target compound along with minor impurities as a white solid. This solid was then washed with methanol to give **S5** as a white crystalline solid (0.30 g, 75%).

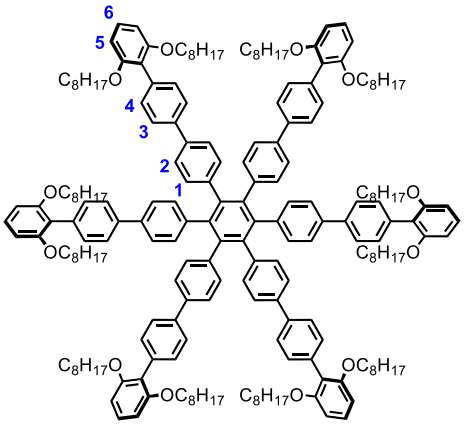

^{1}H NMR (400 MHz, $CDCl_3$) δ 7.47 (d, *J* = 8.4 Hz, 12H, **H_1**), 7.34 (d, *J* = 8.4 Hz, 12H, **H_2**), 7.27 (d, *J* = 8.4 Hz, 12H, **H_3**), 7.18 (t, *J* = 8.3 Hz, 6H, **H_6**), 7.02 (d, *J* = 8.4 Hz, 12H, **H_4**), 6.60 (d, *J* = 8.4 Hz, 12H, **H_5**), 3.86 (t, *J* = 6.6 Hz, 24H, **H_{Oct}**), 1.66 – 1.52 (m, 24H, **H_{Oct}**), 1.37 – 0.84 (m, 156H, **H_{Oct}**).

^{13}C NMR (101 MHz, $CDCl_3$) δ 156.94, 140.57, 139.71, 138.92, 138.05, 132.86, 132.13, 131.42, 125.67, 125.45, 123.40, 111.55, 31.87, 29.36, 29.26, 29.24, 26.06, 24.99, 22.80, 14.27.

MALDI-ToF: *m*/*z* 2984.276 (calculated for $[C_{120}H_{270}O_{12}]^{\bullet+}$ = $[M]^{\bullet+}$: 2984.052).

Compound S6. To a Schlenk flask equipped with a stir bar was added **S5** (200 mg, 67 μmol, 1.0 equiv.), 4,4′-di-tert-butyl-2,2′-dipyridyl (108 mg, 40 μmol, 0.6 equiv.), and $[Ir(COD)OMe]_2$ (133 mg, 20.1 μmol, 0.3 equiv.), and bis(pinacolato)diboron (0.24 g, 0.94 mmol, 14 equiv.). The flask was evacuated and back-filled with N_2 five times, followed by addition of N_2 sparged THF (2.0 mL). This solution was then heated at 65 °C for 18 h. After that, the contents were cooled to room temperature and passed through a bed of celite. After removal of the solvent via rotary evaporation, the resulting red solid was passed through a short SiO_2 plug with $CHCl_3$ to give the target compound along with residual bis(pinacolato)diboron. This solid was then washed several times with methanol and filtered to give **S6** as a white crystalline solid (202 mg, 81%).

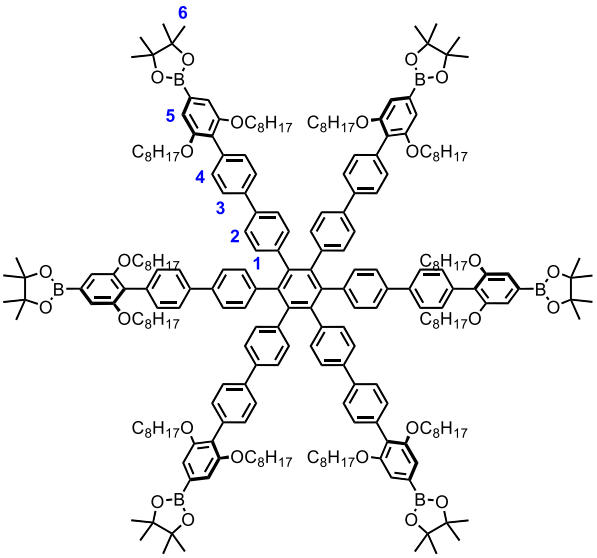

^{1}H NMR (600 MHz, $CDCl_3$) δ 7.45 (d, *J* = 8.5 Hz, 12H, **H_1**), 7.33 (d, *J* = 8.4 Hz, 12H, **H_2**), 7.25 (d, *J* = 7.9 Hz, 12H, **H_3**), 7.03 (s, 12H, **H_5**), 7.00 (d, *J* = 8.3 Hz, 12H, **H_4**), 3.91 (t, *J* = 6.5 Hz, 24H, **H_{Oct}**), 1.76 – 1.52 (m, 24H, **H_{Oct}**), 1.35 (s, 72H, **H_{Oct}**), 1.32 – 0.74 (m, 156H, **H_{Oct}**).

^{13}C NMR (151 MHz, $CDCl_3$) δ 156.94, 140.57, 139.71, 138.93, 138.05, 132.86, 132.13, 131.42, 125.67, 125.45, 123.40, 111.55, 83.92, 68.87, 31.88, 29.36, 29.26, 29.24, 26.06, 25.00, 22.80, 14.27.

MALDI-ToF: *m*/*z* 3741.106 (calculated for $[C_{246}H_{336}B_6O_{24}]^{\bullet+}$ = $[M]^{\bullet+}$: 3740.563).

SUPPORTING INFORMATION

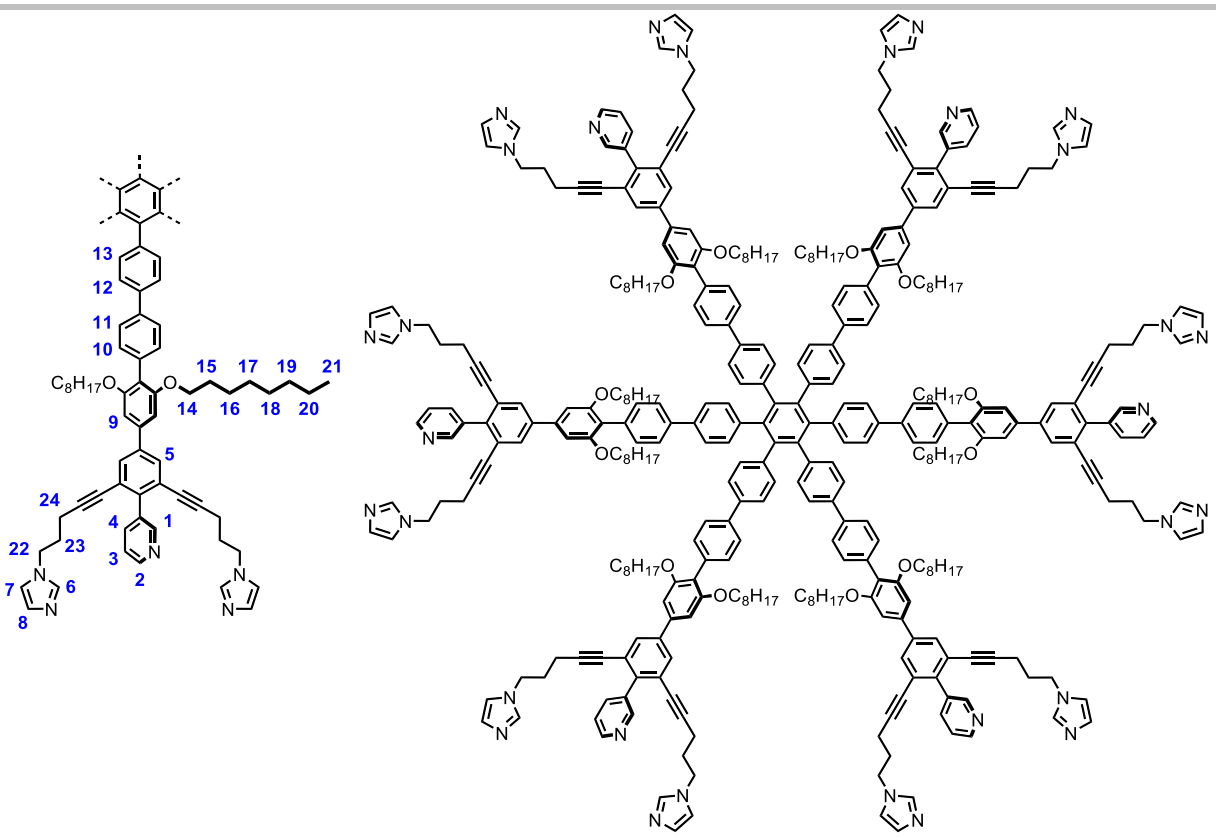

Template T18. To a 50 mL round bottom flask equipped with a stir bar was added **S6** (226 mg, 0.06 mmol, 1.0 equiv.), **T3** (250 mg, 0.55 mmol, 9.0 equiv.), and Pd SPhos G2 (58 mg, 0.07 mmol, 1.2 equiv.). The flask was evacuated and back-filled with N_2 five times, followed by addition of 1,4-dioxane (20 mL). This solution was then vigorously sparged with N_2 for 30 min and it was then placed into an oil bath at 80 °C for 30 min. An N_2 sparged aqueous solution of K_3PO_4 (0.60 mL, 2 M, 1.2 mmol, 20 equiv.) was added, quickly turning the solution to a bright yellow. The reaction was monitored until all starting material was consumed at which the contents were cooled to room temperature and then passed through a bed of celite. After removal of the solvent via rotary evaporation, the resulting yellow/brown oil was then chromatographed (SiO_2, TEA:MeOH:$CHCl_3$ = 1:1:8) to give **T18** (180 mg, 54%) as a tan film.

^{1}H NMR: (600 MHz, $CDCl_3$) δ 8.79 (s, 6H, **H_1**), 8.61 (s, 6H, **H_2**), 7.85 (d, *J* = 7.8 Hz, 6H, **H_4**), 7.69 (s, 12H, **H_5**), 7.52 (d, *J* = 7.8 Hz, 12H, **H_{13}**), 7.48 – 7.28 (m, 48H, **$H_{3,6,11,12}$**), 7.07 – 7.02 (m, 24H, **$H_{8,10}$**), 6.84 – 6.74 (m, 24H, **$H_{7,9}$**), 3.96 (t, *J* = 6.4 Hz, 24H, **H_{14}**), 3.75 (t, *J* = 6.7 Hz, 24H, **H_{22}**), 2.23 (t, *J* = 6.6 Hz, 24H, **H_{24}**), 1.84 – 1.76 (m, 24H, **H_{23}**), 1.67 – 1.61 (m, 24H, **H_{15}**), 1.44 – 1.14 (m, 120H, **$H_{16–20}$**), 0.84 (t, *J* = 6.9 Hz, 36H, **H_{21}**).

^{13}C NMR: (151 MHz, $CDCl_3$) δ 157.79, 157.40, 150.96, 148.93, 141.79, 141.11, 140.57, 139.79, 139.53, 139.03, 137.95, 137.56, 135.61, 132.39, 132.15, 131.51, 130.79, 129.74, 125.77, 125.69, 125.46, 124.06, 122.79, 120.16, 118.98, 105.66, 104.75, 92.32, 80.93, 69.07, 45.16, 31.85, 29.50, 29.34, 29.30, 29.25, 29.21, 29.17, 26.08, 26.04, 22.78, 16.46.

MALDI-ToF: *m/z* 5489.638 (calculated for $[C_{372}H_{408}N_{30}O_{12}] = [M]^{\cdot+}$: 5491.424).

***ls*-P18-Br$_2$**

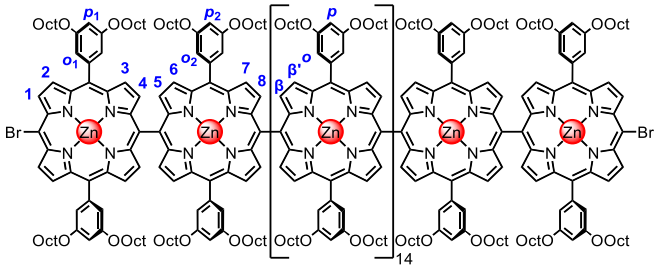

To a stirred solution of ***ls*-P18** (25 mg, 1.3 µmol, 1.0 equiv.) in $CHCl_3$ (5.0 mL) with pyridine (50 µL) in an ice bath (0 °C), a solution of *N*-bromosuccinimide (0.50 mg, 2.8 µmol, 2.1 equiv.) in $CHCl_3$ (1.0 mL) was added dropwise. The reaction was conducted at 0 °C for 5 min, and acetone (0.1 mL) was added to quench the excess *N*-bromosuccinimide. The resulting mixture was purified by flash column chromatography on silica gel using CH_2Cl_2/pentane 1:1 as eluent to give the desired product ***ls*-P18-Br$_2$** (20 mg, 79%).

^{1}H NMR (600 MHz, $CDCl_3$) δ 9.90 (d, *J* = 4.3 Hz, 4H, **H$_1$**), 9.22 (d, *J* = 4.3 Hz, 4H, **H$_2$**), 9.03 – 8.92 (m, 60H, **H$_{β',7}$**), 8.88 (d, *J* = 4.4 Hz, 4H, **H$_6$**), 8.84 (d, *J* = 4.3 Hz, 4H, **H$_3$**), 8.46 – 8.32 (m, 60H, **H$_{β,8}$**), 8.23 (d, *J* = 4.3 Hz, 4H, **H$_4$**), 8.19 (d, *J* = 4.3 Hz, 4H, **H$_5$**), 7.57 – 7.50 (m, 72H, **H$_o$**), 6.86 (s, 4H, **H$_{p1}$**), 6.80 (s, 28H, **H$_p$**), 6.75 (s, 4H, **H$_{p2}$**), 4.33 – 3.98 (m, 144H, **H$_{Oct}$**), 1.99 – 1.68 (m, 144H, **H$_{Oct}$**), 1.59 – 1.10 (m, 720H, **H$_{Oct}$**), 0.96 – 0.73 (m, 216H, **H$_{Oct}$**).

MALDI-ToF *m*/*z* 18819.694 (calculated for $[C_{1152}H_{1476}Br_2N_{72}O_{72}Zn_{18}]^{\bullet+}$ = $(M)^{\bullet+}$: 18820.974).

UV–vis–NIR ($CHCl_3$) λ_{max} (ε / µM^{-1}cm^{-1}): 416 (1.46), 507 (1.56), 587 (1.05) nm.

***ls*-P18-(C$_2$THS)$_2$**

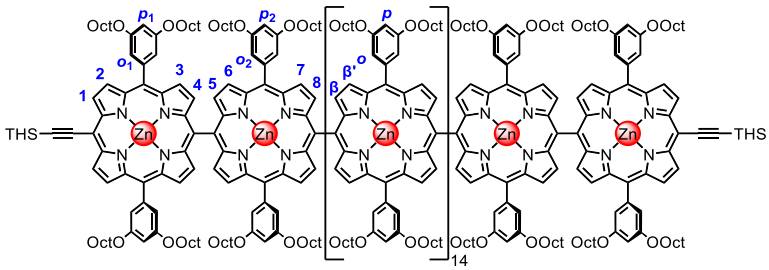

A solution of ***ls*-P18-Br$_2$** (21 mg, 1.1 µmol, 1.0 equiv.) in diisopropylamine (DIPA, 2 mL) and toluene (2 mL) was subjected to freeze-pump-thaw cycles (2). While the solution was still frozen and under argon, $Pd(PPh_3)_4$ (1.3 mg, 1.1 µmol, 1.0 equiv.) and CuI (0.21 mg, 1.1 µmol, 1.0 equiv.) were added, and the contents were subjected to additional freeze-pump-thaw cycles (2). THS-acetylene (4 µL, 3 mg, 10 µmol, 10 equiv.) was added and the reaction mixture was stirred at 50 °C for 3 h. The reaction mixture was filtered through a pad of silica ($CHCl_3$/pentane 1:1) and concentrated under reduced pressure. Purification of the crude by size-exclusion chromatography (S-X1, $CHCl_3$), followed by precipitation from $CHCl_3$/MeOH gave the title compound as a brown powder (20 mg, 93%).

^{1}H NMR (600 MHz, $CDCl_3$) δ 9.88 (d, *J* = 4.3 Hz, 4H, **H$_1$**), 9.19 (d, *J* = 4.3 Hz, 4H, **H$_2$**), 9.14 – 8.92 (m, 60H, **H$_{β',7}$**), 8.86 (d, *J* = 4.4 Hz, 4H, **H$_6$**), 8.80 (d, *J* = 4.4 Hz, 4H, **H$_3$**), 8.47 – 8.31 (m, 60H, **H$_{β,8}$**), 8.24 – 8.16 (m, 8H, **H$_{4,5}$**), 7.64 – 7.40 (m, 72H, **H$_{o,o1,o2}$**), 6.85 (s, 4H, **H$_{p1}$**), 6.84 – 6.73 (m, 28H, **H$_p$**), 6.74 (s, 4H, **H$_{p2}$**), 4.31 – 3.85 (m, 144H, **H$_{Oct}$**), 1.91 – 0.69 (m, 1158H, **H$_{THS,Oct}$**).

MALDI-ToF *m*/*z* 19275.039 (calculated for $[C_{1192}H_{1554}N_{72}O_{72}Si_2Zn_{18}]^{\bullet+}$ = $(M)^{\bullet+}$: 19276.704).

UV–vis–NIR ($CDCl_3$) λ_{max} (ε / µM^{-1}cm^{-1}): 414 (1.46), 507 (1.65), 587 (1.11) nm.

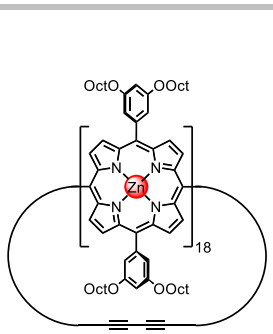

***c*-P18b**

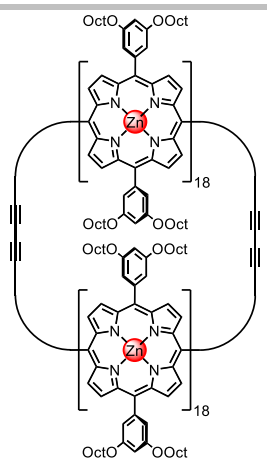

***c*-P36b$_2$**

To a solution of ***l*s-P18-(C$_2$THS)$_2$** (14 mg, 0.73 µmol) in CH_2Cl_2 (6 mL) and $CHCl_3$ (6 mL) was added TBAF (1.4 mL, 1.0 M in THF). After stirring for 1 h, AcOH (1.4 mL) was added, and the reaction mixture was passed through a short pad of silica ($CHCl_3$). Toluene (30 mL) was added to the filtrate, and the chlorinated solvents were removed under reduced pressure. The remaining toluene solution was washed with saturated aq. Na_2CO_3 (3 x 25 mL), H_2O (1 x 25 mL), dried over Na_2SO_4, filtered, and concentrated under reduced pressure. The deprotected 18-mer was passed through a size-exclusion column (Bio-Beads, S-X1, $CHCl_3$). The isolated yield of 18-mer was determined as 12 mg (88%). Deprotected 18-mer (12 mg, 0.64 µmol, 1.0 equiv.) was dissolved in $CHCl_3$ (30 mL) in a 1-L flask and a solution of **T18** (3.5 mg, 0.64 µmol, 1.0 equiv.) in $CHCl_3$ (220 mL) was added. A catalyst mixture was prepared by dissolving CuI (6.1 mg, 32 µmol), $Pd(PPh_3)_2Cl_2$ (4.5 mg, 6.4 µmol), and 1,4-benzoquinone (3.5 mg, 32 µmol) in DIPA (1.0 mL) and $CHCl_3$ (10 mL) using sonication. The catalyst mixture was added to the reaction flask and it was left stirring exposed to air. Progress was monitored by analytical GPC. After 18 hours, trichloroacetic acid (12 mL) was added, turning the contents bright pink/red. The reaction was then transferred to a separatory funnel and washed with H_2O (3 x 25 mL), saturated Na_2CO_3 (3 x 15 mL), brine (1 x 25 mL) and then finally placed over sodium sulfate. Removal of the organics gave a pink/red solid which was then passed through a short size-exclusion column (Bio-Beads S-X1, THF + 1% pyridine), removing unreacted 1,4-benzoquinone (orange band), and concentrated under reduced pressure. Purification by recycling GPC (THF + 1% pyridine), gave demetalated ***c*-P18b** (0.84 mg, 7.4 %) and ***c*-P36b$_2$** (0.36 mg, 4.8%) as pink solids.

Each macrocycle was then remetalated with Zn(II) as follows:

Free-base ***c*-P18b** (0.84 mg) was first dissolved in $CHCl_3$ (2.0 mL). To this solution was then added $Zn(OAc)_2$ (50 mg, 0.73 mmol), followed by MeOH (0.5 mL). This was then stirred for 30 minutes at 25 °C, turning from a pink/red to a brown color. After 30 minutes, the contents were passed through a short size-exclusion column (Bio-Beads S-X1, THF + 1% pyridine) to give Zn-metalated ***c*-P18b** (0.89 mg, 100%) as a brown solid.

Free-base ***c*-P36b$_2$** (0.36 mg) was first dissolved in $CHCl_3$ (2.0 mL). To this solution was then added $Zn(OAc)_2$ (50 mg, 0.73 mmol), followed by MeOH (0.5 mL). This was then stirred for 30 minutes at 25 °C, turning from a pink/red to a brown color. After 30 minutes, the contents were passed through a short size-exclusion column (Bio-Beads S-X1, THF + 1% pyridine) to give Zn-metalated ***c*-P36b$_2$** (0.39 mg, 100%) as a brown solid.

***c*-P18b**:

^{1}H NMR (700 MHz, tetrachloroethane-d_2, 298 K) δ = 10.06–9.94 (m, **H_1**), 9.27–9.17 (m, **H_2**), 9.41–8.49 (m, **$H_{\beta'}$ + H_β**), 8.69–8.63 (m, **H_3**), 8.39–7.92 (m, **H_β**), 7.82–6.98 (m, **H_β + H_o**), 6.99–6.45 (m, **H_p**), 4.36–3.76 (m, -OCH_2- **H_{Oct}**), 2.13–0.98 (m, aliphatic -CH_2- **H_{Oct}**), 0.97–0.70 (m, aliphatic -CH_3 **H_{Oct}**).

UV–vis–NIR ($CDCl_3$, 298 K) λ_{max} (ε / 10^6 $M^{-1}cm^{-1}$): 411 (2.28), 501 (2.72), 578 (1.45), 665 (0.17) nm.

MALDI-ToF *m/z* 18708.401 (calculated for $[C_{1156}H_{1476}N_{72}O_{72}Zn_{18}]^{\bullet+}$ = $(M)^{\bullet+}$: 18709.140).

Retention time: 32.8 min.

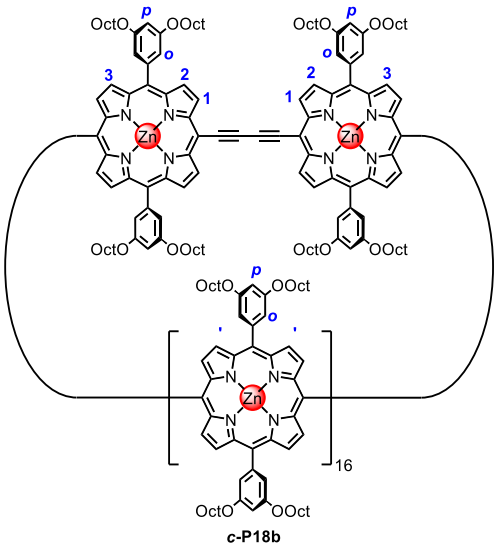

***c*-P36b$_2$**

UV–vis–NIR ($CDCl_3$, 298 K) λ_{max} (ε / 10^6 $M^{-1}cm^{-1}$): 412 (1.55), 498 (1.81), 576 (0.89), 668 (0.083) nm.

MALDI-ToF *m/z* 37420.286 (calculated for $[C_{2312}H_{2952}N_{144}O_{144}Zn_{36}]^{\bullet+}$ = $(M)^{\bullet+}$: 37418.318).

Retention time: 29.4 min.

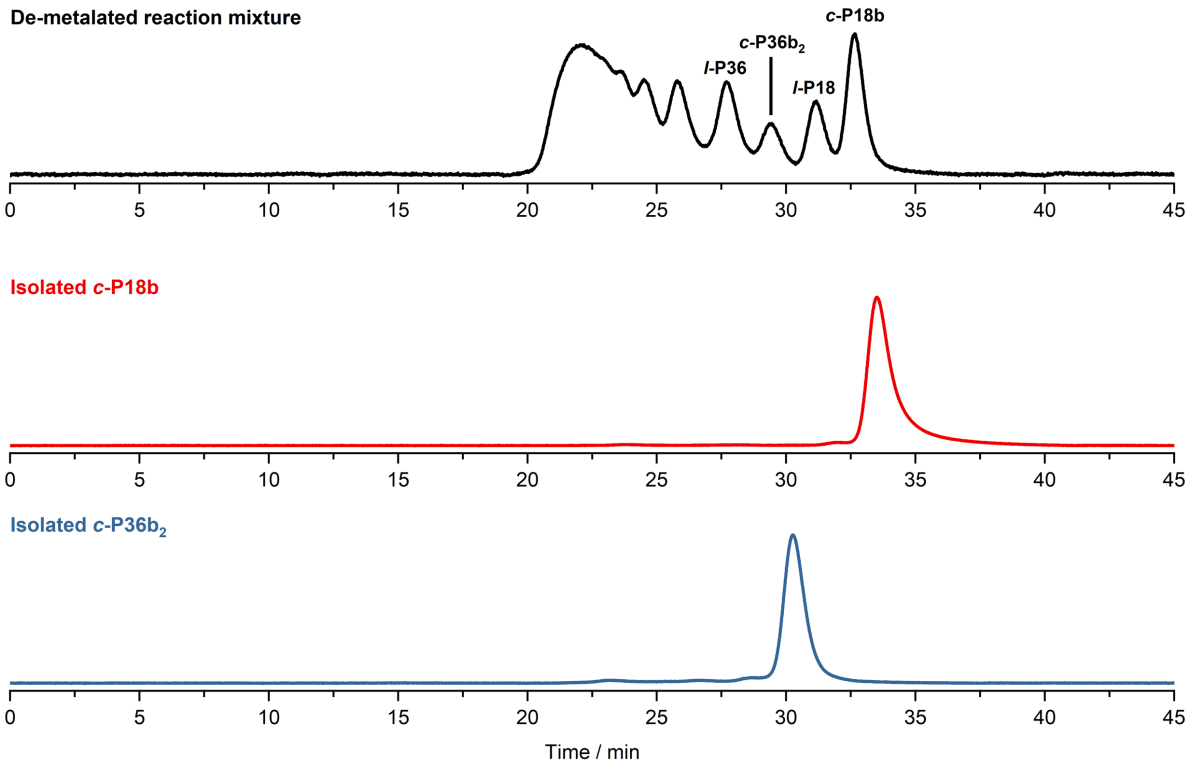

Figure S5. Analytical GPC traces (THF + 1% pyridine, λ = 420 nm). From top to bottom: de-metalated reaction mixture (black), and after insertion of zinc: isolated ***c*-P18b** after GPC (red), and isolated ***c*-P36b$_2$** after GPC (blue). Abbreviated labels ***l*-P18** and ***l*-P36** correspond to unreacted ***l*-P18e** and ***l*-P36be**, respectively. The signals at retention time 20–27 minutes in the GPC trace of the crude reaction mixture indicate the formation of high molecular weight byproducts, which may be linear or cyclic; we have not yet isolated or identified these high molecular weight byproducts.

SUPPORTING INFORMATION

S4 UV–Visible Titrations

All UV-vis titrations were performed in $CDCl_3$ at 298 K. The directly purchased $CDCl_3$ was passed through an alumina plug before the titrations. During a titration, the porphyrin concentration was kept constant by adding porphyrin to the ligand solution. The interaction of the *meso–meso* linked porphyrin trimer ***l*-P3** with ligand **T3** was studied by both formation titration and denaturation titration.

Determination of formation constants from direct formation titrations

The formation constants (K_f) were determined by fitting the binding curves to the 1:1 binding isotherm using the equation:[6]

$$\frac{A-A_0}{A_f-A_0} = \frac{(K_f([P]_0+[L])+1)-\sqrt{(K_f([P]_0+[L])+1)^2-4K_f{}^2[P]_0[L]}}{2K_f[P]_0} \quad \text{(S1)}$$

where A is the observed absorption at a specific wavelength or the difference of absorbance between two wavelengths; A_0 is the starting absorption at this wavelength; A_f is the asymptotic final absorption at this wavelength; [L] is the concentration of ligand (**T3**); [P]$_0$ is the concentration of porphyrin host (***l*-P3**). The fitting analyses were carried out using OriginPro 2020 software.

Determination of formation constants from denaturation titrations

Denaturation (break-up) titrations were performed with competing ligand quinuclidine (**Q**). The denaturation constants (K_{dn}) were determined by fitting the data to the N-dentate denaturation binding isotherm described in the following equation:[6]

$$\frac{A-A_0}{A_f-A_0} = \frac{-K_{dn}[L]^N+\sqrt{K_{dn}{}^2[L]^{2N}+4K_{dn}[L]^N[P]_0}}{2[P]_0} \quad \text{(S2)}$$

where A is the observed absorption at a specific wavelength or difference of absorption between two wavelengths; A_0 is the starting absorption at this wavelength; A_f is the asymptotic final absorption at this wavelength; K_{dn} is the denaturation constant between ligand and porphyrin oligomer complex (***l*-P3·T3**) on titrating with quinuclidine, [L] is the concentration of quinuclidine; [P]$_0$ is the concentration of porphyrin oligomer complex (***l*-P3·T3**), N is the number of binding sites in the complex (N = 3). The fitting analyses were carried out using OriginPro 2020 software.

Followed by determination the denaturation constants (K_{dn}), the formation constants (K_f) can be calculated using the following equation:[7]

$$K_f = \frac{K_Q{}^N}{K_{dn}} \quad \text{(S3)}$$

where N is the number of quinuclidine binding sites involved (N = 3), and K_Q is the formation constant of the porphyrin monomer (**P1**) and quinuclidine in $CDCl_3$. The value log K_Q = 5.59 ± 0.03 was determined in $CDCl_3$ at 298 K by direct formation reference titration and reported previously.[5]

Formation titrations

The binding curves were fitted with equation S1 to give the formation constant log K_f = 7.60 ± 0.01.

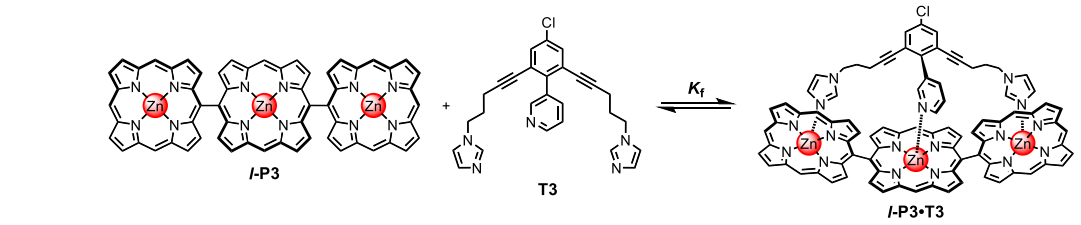

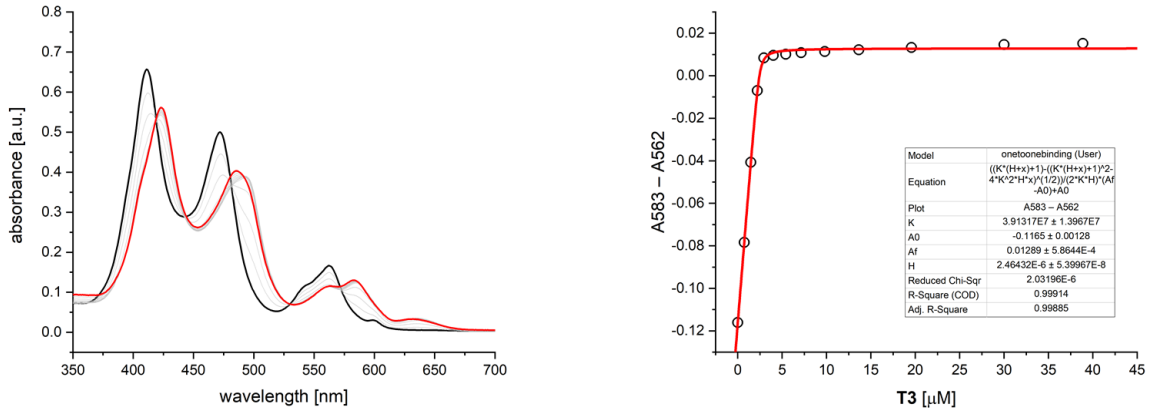

Figure S6. UV–vis formation titration with ***l*-P3** and **T3** ($CDCl_3$, 298 K, [***l*-P3**] = 3.0 × 10^{-6} M, K_f = 3.9 × 10^7 M^{-1}, R^2 = 0.99885).

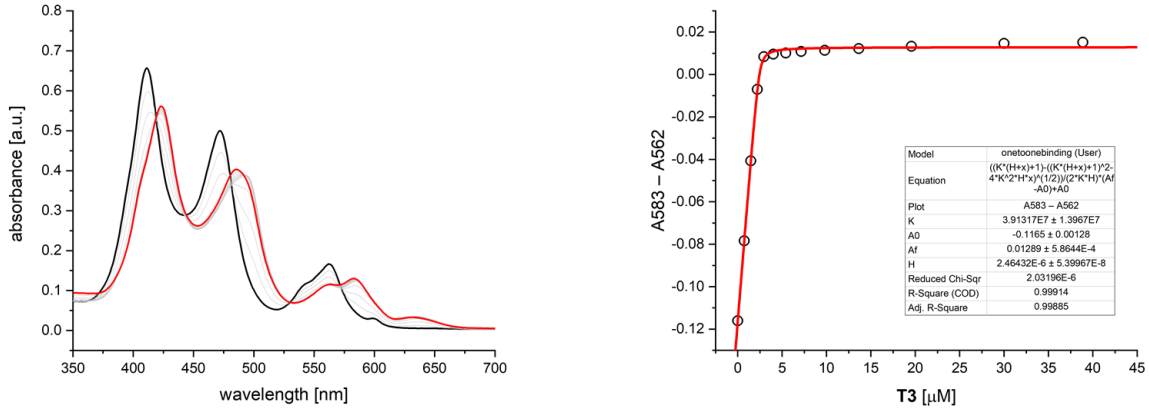

Figure S7. UV–vis formation titration with ***l*-P3** and **T3** ($CDCl_3$, 298 K, [***l*-P3**] = 2.5 × 10^{-6} M, K_f = 4.1 × 10^7 M^{-1}, R^2 = 0.99824).

SUPPORTING INFORMATION

Denaturation titrations

Table S1. Summary of the denaturation constants (K_{dn}) and formation constants (K_f) determined by denaturation titrations.

	log K_{dn}[a]	log K_f[b]
Run 1	8.25	8.52 ± 0.09
Run 2	8.28	8.49 ± 0.09
Average ± S.D.	8.27 ± 0.02	8.51 ± 0.11[c]

[a] The denaturation constants were estimated by fitting the binding curves to equation S2.
[b] The formation constants were calculated using equation S3.
[c] Errors were determined by propagating the errors from the K_Q values used.

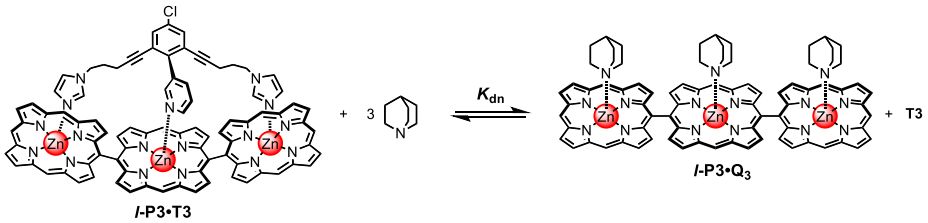

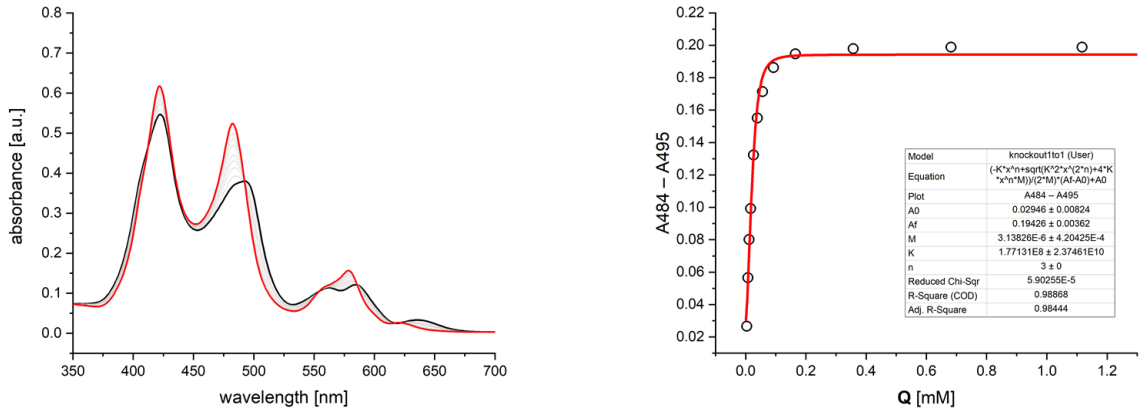

Figure S8. UV–vis denaturation titration with ***I*-P3·T3** and **Q** ($CDCl_3$, 298 K, [***I*-P3·T3**] = 3.0 × 10^{-6} M, K_{dn} = 1.8 × 10^8 M^{-2}, R^2 = 0.98444).

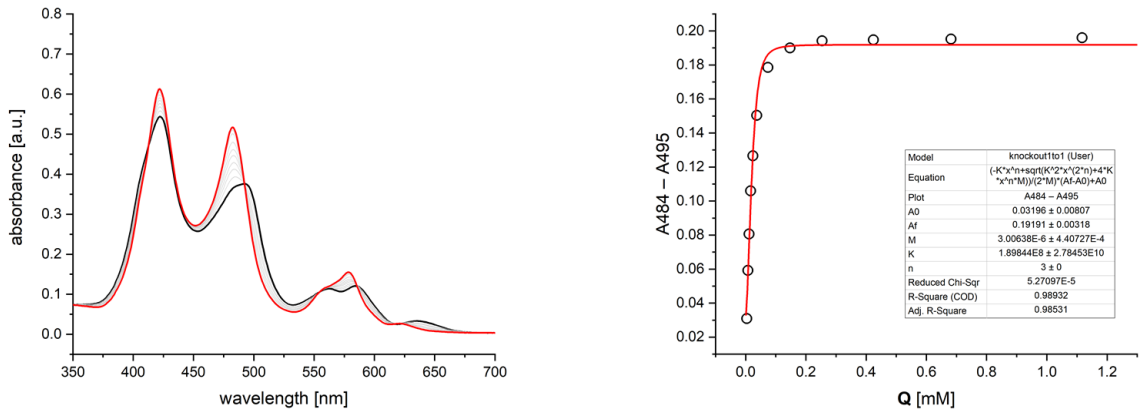

Figure S9. UV–vis denaturation titration with ***I*-P3·T3** and **Q** ($CDCl_3$, 298 K, [***I*-P3·T3**] = 3.0 × 10^{-6} M, K_{dn} = 1.9 × 10^8 M^{-2}, R^2 = 0.98531).

SUPPORTING INFORMATION

S5 Computational Modeling

Calculated molecular xyz coordinates from molecular dynamics simulations, StrainViz calculations and screening of ligand designs relating to this article are openly available in Zenodo, DOI: 10.5281/zenodo.10451590.

Modelling of tridentate ligands. DFT calculations were performed using the Gaussian 16/A.03 suite of programs.[8] Geometries were optimized at the PBE0-D3(BJ)/Def2SVP level of theory.[9,10] The PBE0 hybrid functional and D3(BJ) dispersion correction were invoked with the "PBE1PBE" and "GD3BJ" keywords in Gaussian 16. A series of tridentate ligands (Figure S10) and their complexes with the zinc porphyrin trimer ***l*-P3** were optimized. Aryl groups at the *meso* positions of ***l*-P3** were replaced with hydrogens. Binding energies were estimated at the same level of theory by subtracting the calculated electronic energies according to:

$$E_{binding} = E(\textit{l}\text{-P3}\cdot\text{T3a}) - (E(\textit{l}\text{-P3}) + E(\text{T3a})) \quad \text{(S4)}$$

Note that these calculations only served to provide approximate binding energies of the ligands with ***l*-P3**, for selecting a suitable ligand component in **T18**. The systems were calculated in vacuum and no basis set superposition error correction was applied.

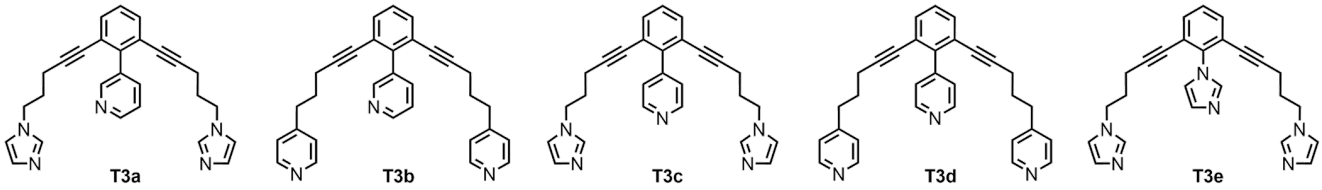

Figure S10. Chemical structures of ligands that were screened.

Table S2. List of electronic energies and calculated binding energies.

	Energy / Hartrees	Binding energy / kJ mol^{-1}
***l*-P3**	–8294.373	
T3a	–1545.790	–313.72
***l*-P3·T3a**	–9840.282	
T3b	–1589.838	–281.74
***l*-P3·T3b**	–9884.318	
T3c	–1545.794	–296.50
***l*-P3·T3c**	–9840.280	
T3d	–1589.842	–275.09
***l*-P3·T3d**	–9884.319	
T3e	–1523.769	–305.42
***l*-P3·T3e**	–9818.258	

Strain calculations by DFT and molecular mechanics. All the DFT calculations were performed using Gaussian 16/A.03.[8] The porphyrin *meso* aryl groups were replaced with hydrogen atoms. Geometries of molecular models ***c*-P18** and ***c*-P18b** were optimized at PBE0-D3(BJ)/Def2SVP level of theory.[9,10] Geometry optimizations of ***l*-P4**, ***l*-P5**, ***l*-P4b$_3$e** and ***l*-P5b$_4$e** were detailed in ref. 5. Optimization of all the geometries using molecular mechanics was also reported in ref. 5.

The theoretically predicted strain energies (E_{strain}) were estimated from the homodesmotic reactions shown in Figure S11, where the calculated electronic energies were subtracted according to:

$$E_{\boldsymbol{c-PN}} + N * E_{\boldsymbol{l-P4}} - N * E_{\boldsymbol{l-P5}} = E_{strain(\boldsymbol{c-PN})} \quad \text{(S5)}$$

$$E_{\boldsymbol{c-PNb}} + (N-1) * E_{\boldsymbol{l-P4}} + E_{\boldsymbol{l-P4b3e}} - N * E_{\boldsymbol{l-P5}} - E_{\boldsymbol{l-P5b4e}} = E_{strain(\boldsymbol{c-PNb})} \quad \text{(S6)}$$

SUPPORTING INFORMATION

Table S3. Optimized energies and strain energies for the cyclic and linear oligo porphyrin compounds.

	DFT calculations		molecular mechanics calculations	
Compound	**Energy / Hartrees**	**Strain energy / kJ mol^{-1}**	**Energy / kJ mol^{-1}**	**Strain energy / kJ mol^{-1}**
***l*-P4**	–11058.770946	—	–2460.387	—
***l*-P5**	–13823.169308	—	–3045.522	—
***l*-P4b$_3$e**	–11666.853741	—	–3365.366	—
***l*-P5b$_4$e**	–14583.279225	—	–4131.126	—
***c*-P18**	–49759.130163	105.9	–13677.766	105.9
***c*-P18b**	–49911.160297	98.0	–13503.486	99.6

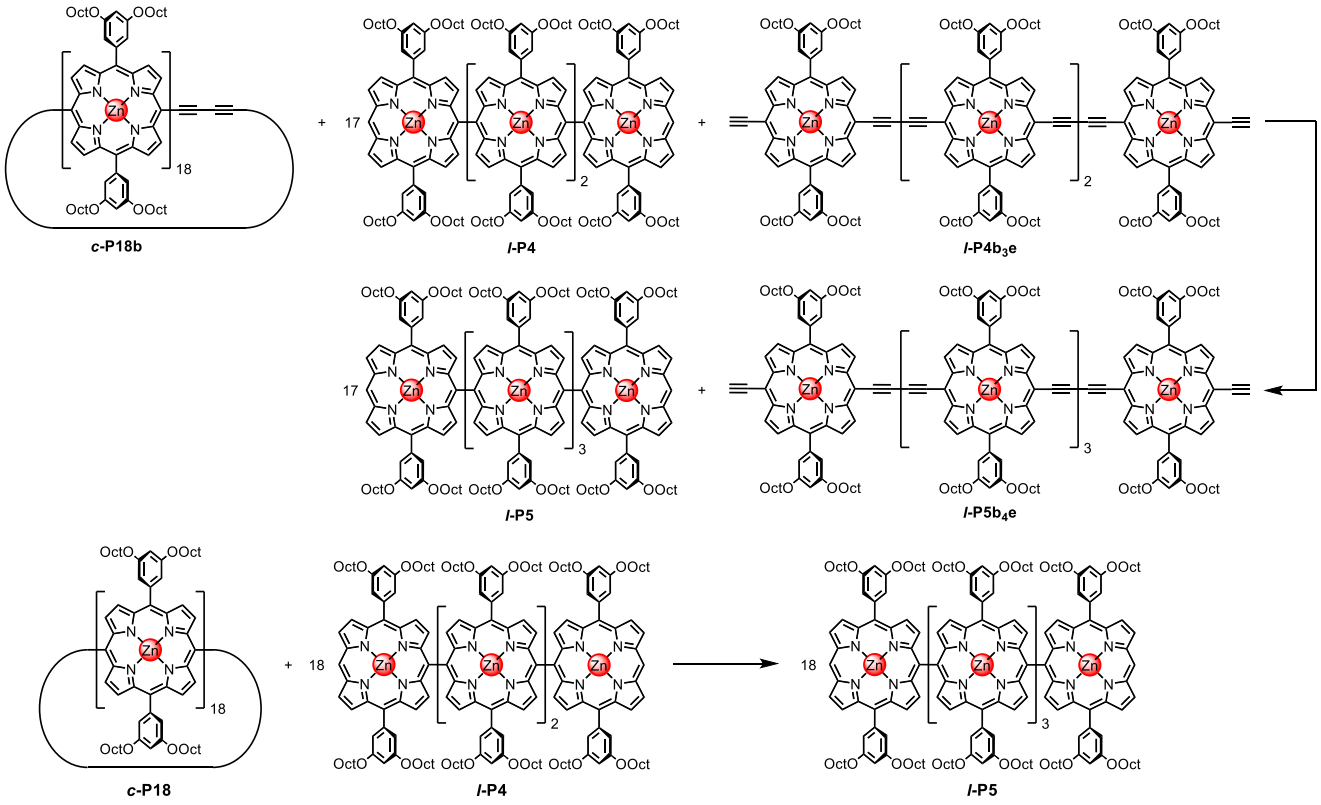

Figure S11. Homodesmotic reaction scheme used for the strain calculations for ***c*-P18** and ***c*-P18b**.

StrainViz calculation. Calculations to visualize the ring strain present in ***c*-P18b** and ***c*-P6b$_6$** was done according to the method outlined by Jasti and coworkers.[11] whereby the optimized cyclic structure is cut into non-cyclic fragments which are then individually optimized. The forces acting on the internal coordinates during the geometry optimizations are used to estimate the strain energy present in the bonds, angles and dihedral angles of the original structure. Due to the large size of molecules studied here and the number of optimizations required for this approach, we carried out calculations at a semi-empirical (XTB) level of theory, instead of the DFT level used in previous work.

The cyclic structures were optimized using ORCA 5.0[12] together with the XTB software package.[13] Fragments were generated by removing two adjacent porphyrins, and these fragments were then optimized at the XTB level of theory. Additional internal coordinates were defined for the butadiyne motifs because the ORCA geometry optimization algorithm is unstable for systems with large numbers of co-linear atoms. The resulting strain from the 'auxiliary' internal coordinates that did not correspond to actual bonds of the structure was spread over the bonds that lie between the atoms that make up that 'auxiliary' internal coordinate.

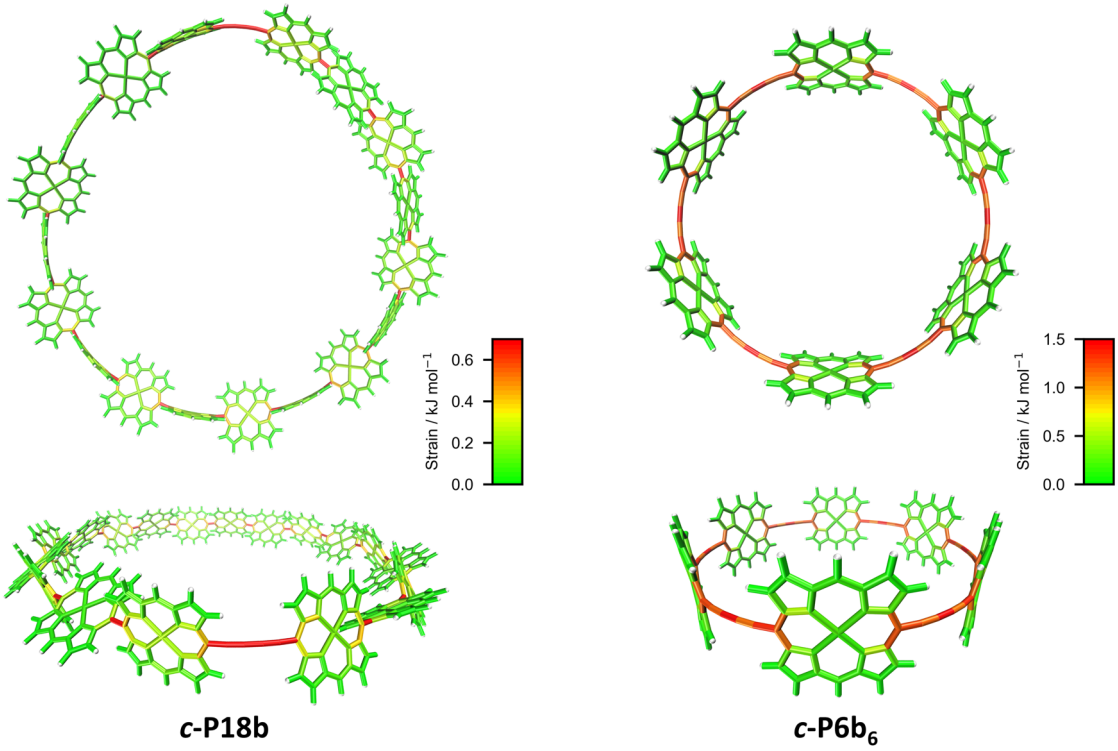

Figure S12. StrainViz representations of the strain in **c-P18b** and **c-P6b$_6$**. The color scales were chosen to visualize strain in the porphyrins and *meso-meso* bonds. The butadiynes have strains greater than the maximum strain of the color bar.

The total amount of strain energy calculated this way is comparable to that from homodesmotic reactions calculated using DFT at the PBE0-D3(BJ)/def2-SVP level of theory: ***c*-P18b** has a strain energy of 110.2 kJ/mol compared to 98.0 kJ/mol from DFT, and ***c*-P6b$_6$** 98.7 kJ/mol compared to 99.8 kJ/mol from DFT.

The StrainViz images (Figure S12) show that the strain is greatest in the butadiyne bridges and the *meso-meso* bonds connecting porphyrins. However, while the strain is most concentrated in the butadiynes, the majority of the strain is spread over the many bonds in the porphyrin units, with 83% of the strain in ***c*-P18b** and 60% in ***c*-P6b$_6$** still residing on the porphyrins. All the porphyrin units in ***c*-P6b$_6$** carry equal strain, whereas the distribution in ***c*-P18b** is uneven. The amount of strain alternates, with larger amounts of strain on porphyrins that face the center of the ring (such as the porphyrins adjacent to the butadiyne link) and smaller amounts on those that are parallel to the overall ring plane as they are less easily distorted (Figure S13). The difference in strain between adjacent porphyrins decreases in the center of the ring further away from the butadiyne link where porphyrins are less well aligned with the overall ring plane. Porphyrins closer to the butadiyne line are less strained than ones further in the center of the ring as more of the curvature is taken up by the alkyne bonds.

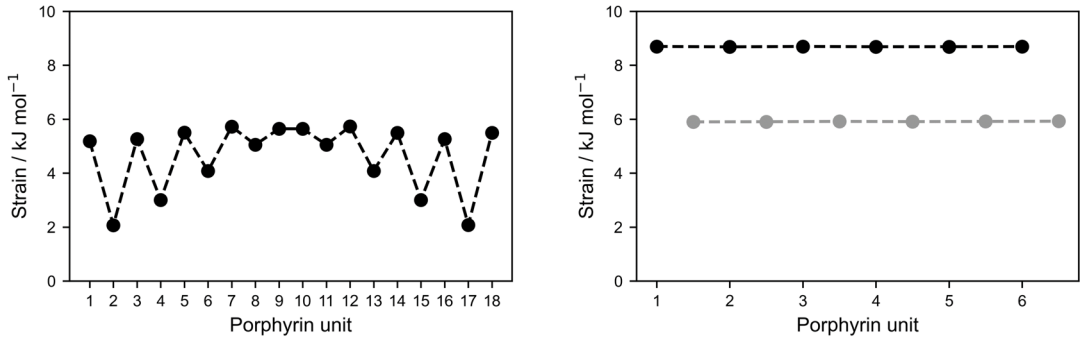

Figure S13. Distribution of strain across the porphyrins (black) in ***c*-P18b** (left) and ***c*-P6b$_6$** (right). Strain on butadiyne bonds in grey. The porphyrin units in ***c*-P18b** are numbered such that porphyrins 1 and 18 neighbor the butadiyne link.

SUPPORTING INFORMATION

Parameterization for Molecular Dynamic Simulations. Parameters for the porphyrin oligomers are equivalent to those published in our previous work.[5] The template was parameterized with the General Amber Force Field (GAFF) using the LEaP programme (AMBER20 tools).[14] Adjustment of the dihedral angle parameters of the central benzene unit was necessary because GAFF is not able to correctly assign atom types in a hexaphenylbenzene structure (i.e., it underestimates the dihedral angles of the benzene unit which leads to unrealistic "buckling" of the ring). To prevent this, any dihedral angle where the two central atoms are part of the central benzene were set to the dihedral angle parameters of the benzene unit in C_6H_6.

Molecular Dynamic Simulations. All molecular dynamics (MD) simulations were performed in an isothermal-isobaric (NPT) ensemble at 300 K and 1 bar with a time step of 2 fs using GROMACS (v. 2019.2).[15] Simulations employed the General AMBER force field[16] with modifications to parameters for zinc ions and porphyrin connections as described above. Systems were minimized using the steepest descent algorithm for 5000 steps or until the maximum force on any atom was below 1000 kJ mol^{-1} nm^{-1} and subsequently equilibrated using a velocity-rescaling thermostat[17] and Parrinello-Rahman barostat.[18] All simulations were performed in explicit chloroform[19] with three-dimensional periodic boundary conditions. The box sizes were chosen by leaving 1 nm distance between solute and box boundary. Long-range electrostatic interactions were calculated using the particle mesh Ewald method.[20] All bond lengths involving hydrogen atoms were constrained with the LINCS algorithm.[21] All MD simulations were performed with the complete molecule, including 3,5-bis(octyloxy)phenyl solubilizing groups.

Flexibility of *c*-P18b. Molecular dynamics simulations of ***c*-P18b** were run for 300 ns with and without the template **T18**. They indicate a much lower degree of flexibility of the porphyrins compared to the previously simulated ***c*-P24b** ring (see Figure S14). No full rotation of any porphyrin in the ***c*-P18b** ring was observed over the course of a 300 ns simulation, while the simulation for ***c*-P24b** displayed multiple flips back and forth for each porphyrin. This results in a unimodal distribution of dihedral angles in the ***c*-P18b** ring whereas the ***c*-P24b** ring produced bimodal distribution of dihedral angles due to the symmetry of the porphyrins and their comparatively free rotation (see Figure S14e). As expected, introduction of a template further restricts rotation of the porphyrin units and therefore results in more static relative orientations between porphyrins and a narrower distribution of dihedral angle (see Figure S14d and S14e).

Viability of ring-closure reactions. Distance and angle plots of the terminal ethynes of the unclosed complex have previously been used to assess the feasibility of a ring closure reaction.[5] Simulations of the ***l*-P18e·T18** complex have been used to sample end-to-end distances and angles and are shown in Figure S15. The 18-mer complex has a smaller average end-to-end distance than the previously investigated ***l*-P24e·(T12)$_2$** with an average distance of 9.94 Å compared to 14.8 Å for the latter. However, the closest approach of the end groups is similar with 3.36 Å for the 18-mer complex and 3.22 Å for the 24-mer complex. The 2D histogram in Figure S15b also shows a stronger correlation between the end-to-end distance and angle for the 18-mer than for the 24-mer. In the 18-mer complex a larger distance is more likely to be associated with a smaller angle as the main mechanism by which the ends move away from each other is in the direction of an opening of the ring because the single template holds the ***l*-P18e** oligomer flat in one plane (covariance = –0.22). The 24-mer on the other hand has less correlation between distances and angles because the binding by two templates does not keep the ***l*-P24e** oligomer necessarily flat in one plane and the main mechanism by which the ends move away from each other is by displacement away from the mean plane of the complex (covariance = 0.09).

Figure-of-eight structure of *c*-P36b$_2$·(T18)$_2$. In addition to the ***c*-P18b** ring, the ring-closure reaction also yielded the ***c*-P36b$_2$** ring resulting from macrocyclization of two ***l*-P18e** units. Molecular dynamics **s**imulations were run for 100 ns to assess the stability of the ***c*-P36b$_2$·(T18)$_2$** figure-of-eight complex and to investigate its structure (see Figure S16). The distance between chains at the cross-over point of the figure-of-eight structure was defined as the distance between the centers of mass of the butadiyne units and is spread between 1 and 2 nm with an average distance of 1.57 nm (compared to a ring diameter of 4.7 nm). The planes of the two rings have a significant angle between them (average angle of 51.9°).

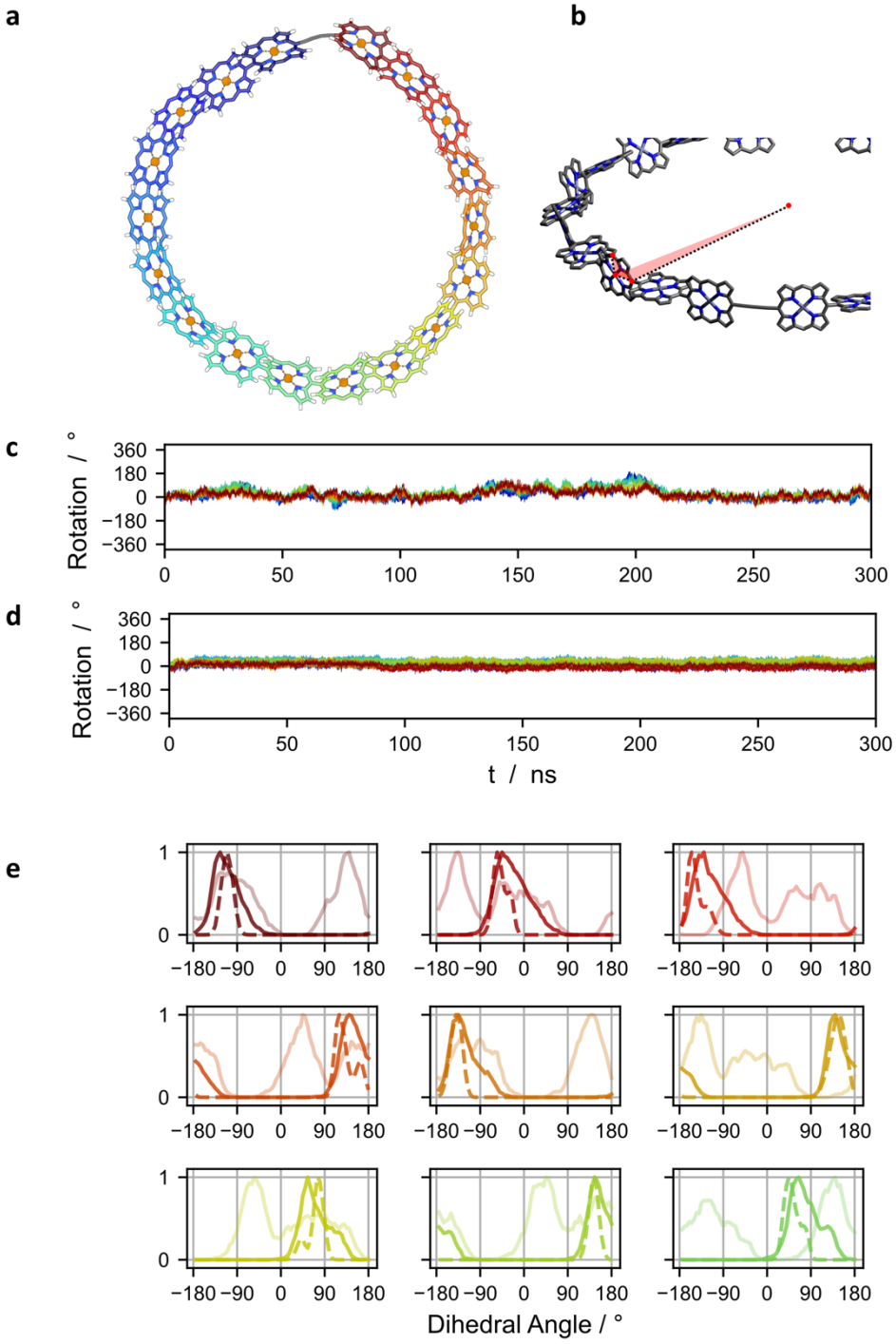

Figure S14. Flexibility of porphyrins in ***c*-P18b**. (a) Structure of ***c*-P18b** with color-coding used in the remaining figure (sidechains have been removed for clarity in image). (b) Definition of the dihedral angle by the center of mass of the ring, a *meso*-C that connects to another porphyrin, the zinc atom and a *meso*-C connecting to a side chain. (c) Rotation of porphyrins relative to t = 0 for the free ring. (d) Rotation of porphyrins relative to t = 0 for the template complex ***c*-P18b·T18**. (e) Histograms of the dihedral angle distribution for the first 9 porphyrins (other half equivalent by symmetry); solid line shows free ring, dashed line shows template complex and faint line shows the dihedral angle distribution in the free ***c*-P24b** ring for reference.

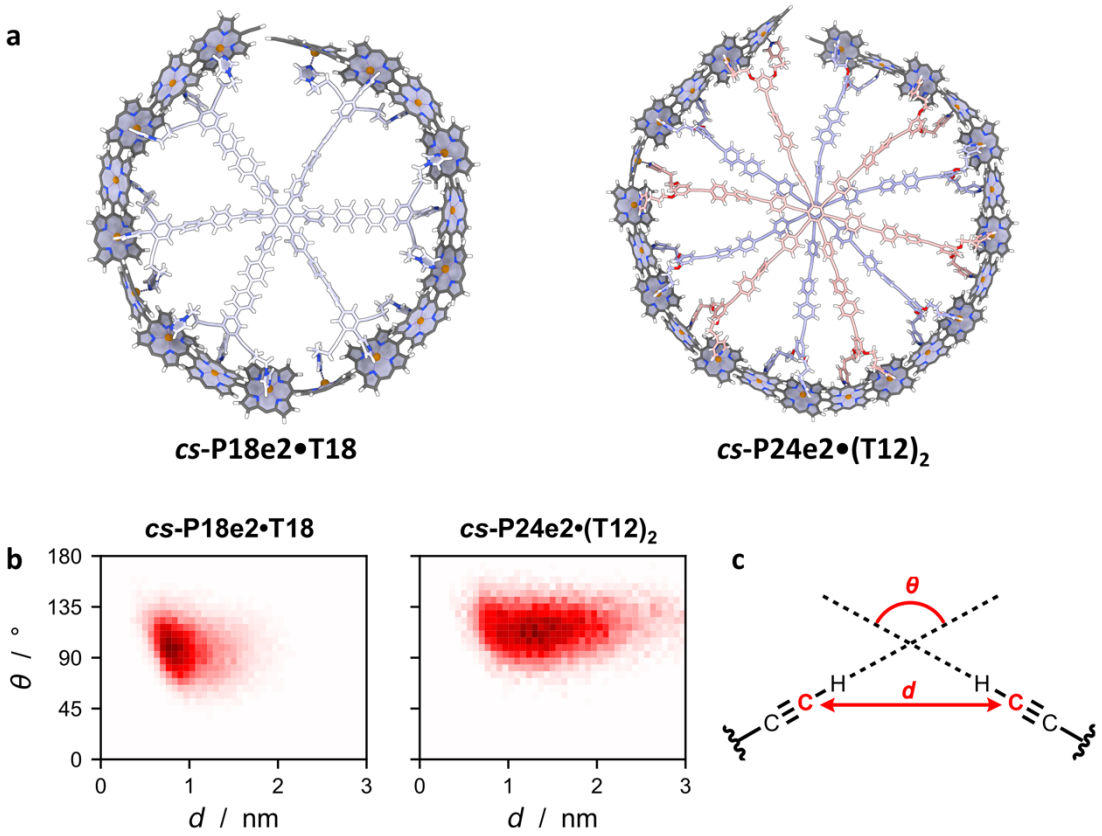

Figure S15. (a) Structure of ***l*-P18e·T18** and ***l*-P24e·(T12)$_2$** complexes. (b) 2D histogram plots of end-to-end distances and angles. (c) Definition of the end-to-end distance and angle.

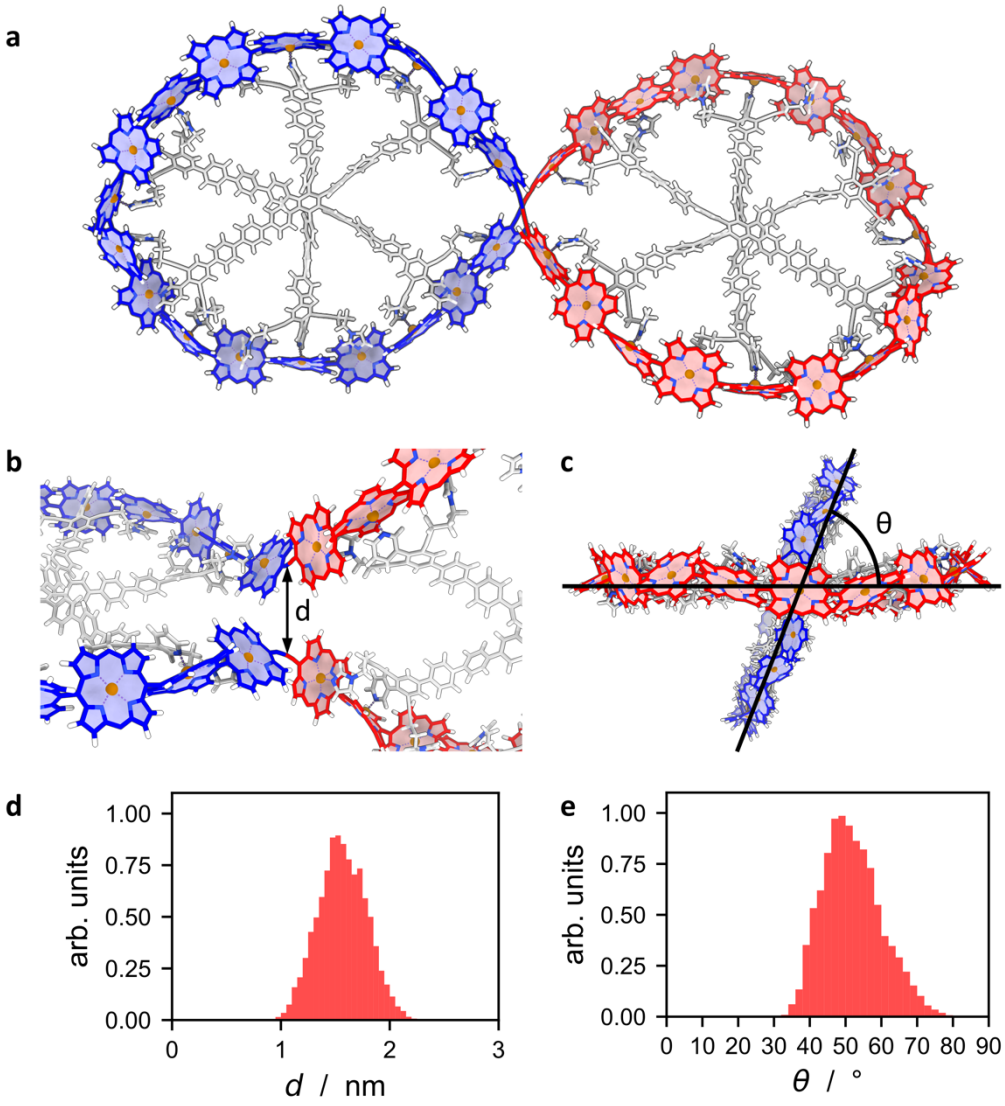

Figure S16. (a) Figure-of-eight structure of ***c*-P36b$_2$·(T18)$_2$** complex with the sections originating from two different ***l*-P18e** fragments color-coded in red and blue, and templates in white. (b) Distance between two butadiyne units plotted in histogram (d). (c) Angle between average ring planes plotted in histogram (e). The average angle between planes of the two half rings is of 51.9°.

SUPPORTING INFORMATION

S6 Scanning Tunnelling Microscopy

STM details. All STM images were acquired with an Omicron STM-1 system operating under ultra-high vacuum (UHV) conditions with a base pressure of 2 × 10^{-9} mbar. Images were acquired at room temperature in constant current mode using electrochemically etched tungsten tips, coated in gold during tip optimization. Image acquisition parameters (sample bias and current set-point) are stated within figure captions.

Au(111) on mica surfaces (Georg Albert PVD GmbH) were prepared by cycles of Ar ion sputtering (0.76 keV for 20 minutes at a pressure of 9 × 10^{-6} mbar) and annealing (~500 °C, 20 minutes). Samples were transported between the STM and XPS UHV systems using a vacuum suitcase at a pressure of < 1 x 10^{-10} mbar.

Electrospray deposition. ***c*-P18b**, ***c*-P24b** and ***c*-P36b$_2$** were synthesized as outlined above and deposited upon a clean Au(111) substrate via electrospray ionization (Molecularspray Ltd, UHV4i source). 50 µg/mL solutions of ***c*-P18b**, ***c*-P24b** and ***c*-P36b$_2$** in toluene/methanol (3:1 ratio) were prepared. ***c*-P18b** was deposited with a solution flow rate of 0.1 mL/hour for 40 minutes using a potential of 1.9 kV to initiate the electrospray event (base pressure during deposition was 1 x 10^{-7} mbar). ***c*-P24b** was deposited with a solution flow rate of between 0.1 and 0.03 mL/hour for 30 minutes using a potential of 1.2 kV to initiate the electrospray event (base pressure during deposition was 2.5 x 10^{-7} mbar). ***c*-P36b$_2$** was deposited with a solution flow rate of between 0.1 and 0.03 mL/hour for 20 minutes using a potential of 1.9 kV to initiate the electrospray event (base pressure during deposition was 1 x 10^{-7} mbar).

Nanoring characterization via STM. Nanoring dimensions were measured from line profiles acquired along the long- and short-axis of the rings; as shown in Figure S17. Peak-to-peak measurements were obtained to determine the separation between the features corresponding to the position of the nanoring circumference. Measurements were performed on data acquired with both 'forward' and 'backward' scan directions. An average of the two measurements was taken, to minimize the effect of drift. The circumference of the rings was estimated using the Ramanujan approximation for the circumference of an ellipse:

$$C \approx \pi[3(a+b) - \sqrt{(3a+b)(a+3b)}] \quad \text{(S7)}$$

where C is the circumference of the ellipse, with a and b being the radii of the long- and short-axis of the ellipse, respectively.

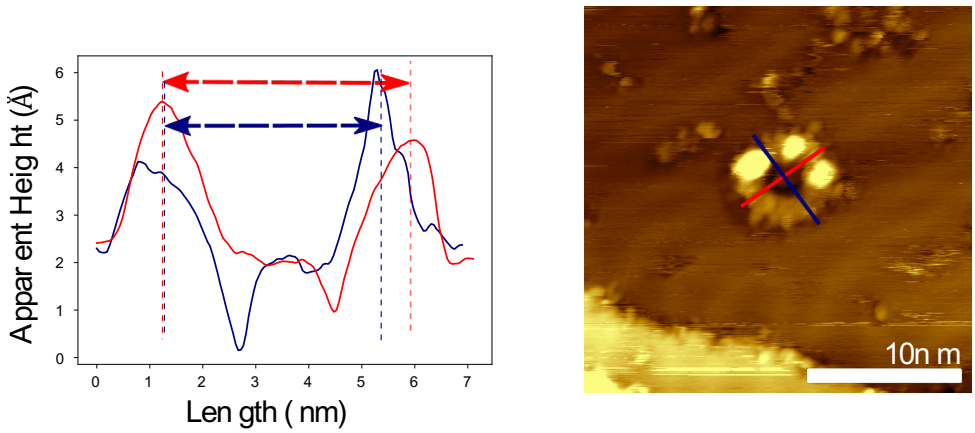

Figure S17. Line profiles acquired for the long- and short-axis of ***c*-P24b** (line-profile locations are indicated within the STM image). The peak-to-peak separation on the red and blue line profiles are 6.2 nm and 5.7 nm, respectively. The STM image is of ***c*-P24b** on Au(111) following electrospray deposition (Sample bias = –1.8 V, Set-point current = 20 pA).

SUPPORTING INFORMATION

Characterization of *c*-P18b, *c*-P24b and *c*-P36b$_2$ dimensions

Using the method previously described, the dimensions of ***c*-P18b**, ***c*-P24b** and ***c*-P36b$_2$** were obtained following deposition onto Au(111); as demonstrated in Figure S18 (Figure S18a shows ***c*-P18b**, Figure S18b ***c*-P24b**, and Figure S18c ***c*-P36b$_2$**). The average dimensions of the nanorings were measured as follows: ***c*-P18b** circumference = 12 ± 1 nm, long axis = 4.3 ± 0.5 nm, short axis = 3.4 ± 0.5 nm. ***c*-P24b** circumference = 18 ± 1 nm, long axis = 6.9 ± 0.9 nm, short axis = 4.3 ± 0.7 nm. ***c*-P36b$_2$** circumference = 24 ± 3 nm, long axis = 8.9 ± 1.4 nm, short axis = 6.0 ± 1.3 nm. The number of induvial rings measured for ***c*-P18b**, ***c*-P24b** and ***c*-P36b$_2$** is 41, 38 and 59 respectively.

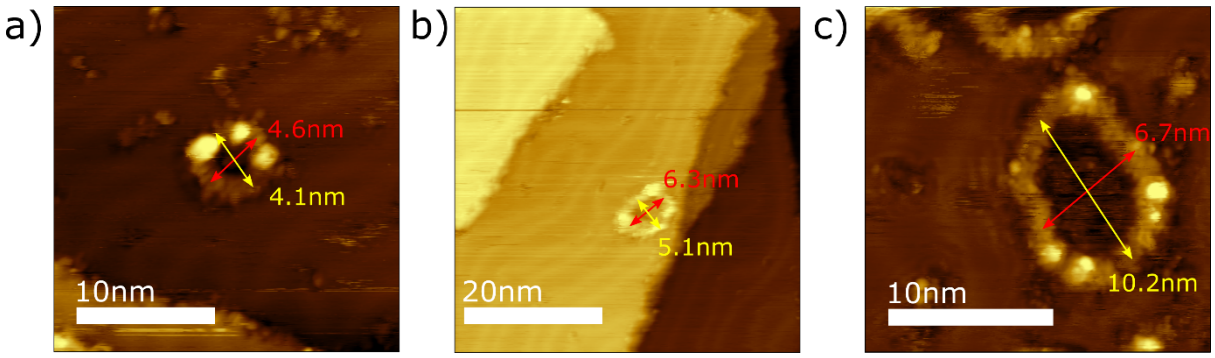

Figure S18. STM image of (a) ***c*-P18b**, (b) ***c*-P24b**, and (c) ***c*-P36b$_2$** deposited onto Au(111) via electrospray deposition. Measurements for the statistical analysis of the ring dimensions were acquired from these types of image (measurement positions indicated by red and yellow arrows). Imaging parameters: (a and c) Sample bias = –1.8 V, Set-point current = 15 pA. (b) Sample bias = –1.8 V, Set-point current = 20 pA.

The dimensions of the long- and short-axis of ***c*-P18b**, ***c*-P24b** and ***c*-P36b$_2$** were acquired following electrospray deposition on to separate Au(111) substrates. Figure S19 displays the measured dimensions as well as the average circumference (as estimated by the Ramanujan approximation) for each species and black solid/dashed lines representing flattening factor, *f*:

$$f = \frac{a-b}{a} \tag{S8}$$

where *a* and *b* are the long and short, respectively, radii of the ellipse defined for each nanoring species. The three nanoring species clearly display three distinct values for the average circumference: 12 ± 1 nm, 18 ± 1 nm, and 24 ± 3 nm for the ***c*-P18b**, ***c*-P24b** and ***c*-P36b$_2$** nanorings**,** respectively. It is also evident, from the estimated values of circumference, that the ***c*-P36b$_2$** nanoring material contains small quantities of the smaller nanorings (***c*-P18b** and ***c*-P24b**). The majority of the ***c*-P18b** species have a flattening factor of $f < 0.4$ (indicating some deviation from circularity) with the ***c*-P24b** and ***c*-P36b$_2$** species showing increased flattening ($f < 0.6$ in the majority of cases) due to the increased flexibility of the larger rings (as seen in Figure S19).

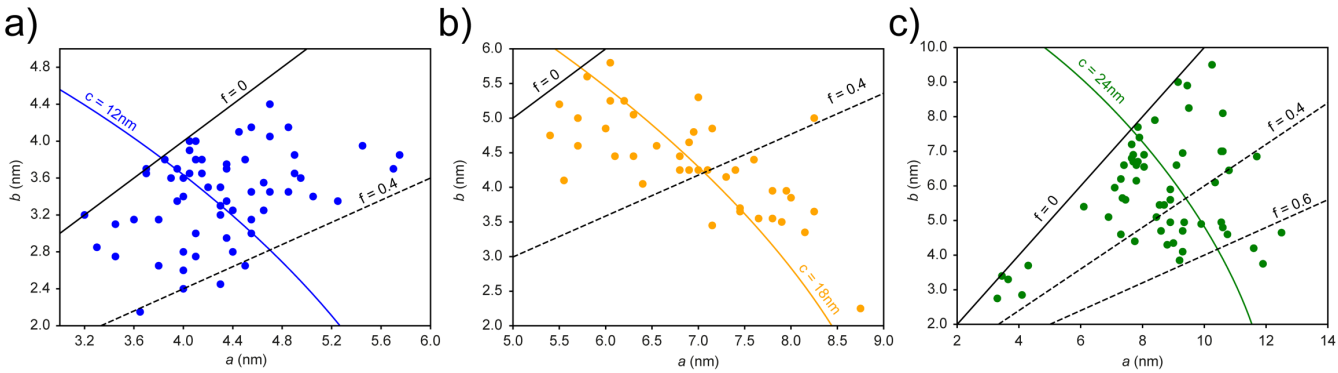

Figure S19. Graph showing the experimentally measured long- and short-axis for (a) ***c*-P18b**, (b) ***c*-P24b** and (c) ***c*-P36b$_2$** nanorings deposited on to Au(111). The blue, yellow, and green arcs represent the ellipses of fixed circumference equivalent to an average circumference of 12 nm, 18 nm, and 24 nm, respectively. In all cases, the solid black line represents a flattening ratio of 0, indicating a circular ring shape. The dotted lines represent flattening ratios of 0.4 and 0.6, the shape becoming more elliptical with increasing *f* value.

SUPPORTING INFORMATION

Overview of surface following electrospray deposition

Sub-monolayer coverages of ***c*-P18b**, ***c*-P24b** and ***c*-P36b$_2$** were obtained following electrospray deposition. Figure S20 shows several large-area images demonstrating the presence of individual molecules and small clusters of nanorings, as well as some amounts of linear materials (assigned to cleaved nanorings).

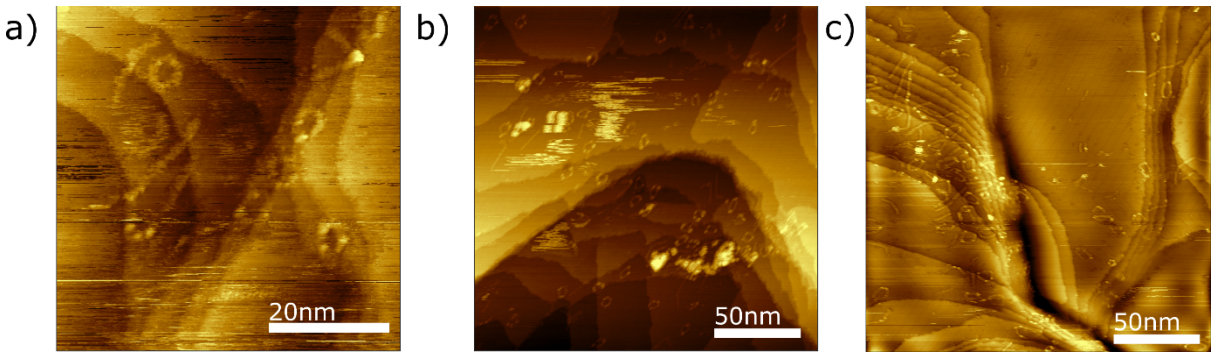

Figure S20. The distribution of (a) ***c*-P18b**, (b) ***c*-P24b**, and (c) ***c*-P36b$_2$** on Au(111) following electrospray deposition. Image parameters: Sample bias = –1.8 V, Set-point current = 20 pA. Image (c) has been 'flattened' via the removal of a polynomial background, artificially levelling the image to provide sufficient contrast to identify the rings species on Au(111) terraces at several heights.

Statistical information was acquired as to the number of intact/whole nanorings that could be identified, as well as the number of broken species characterized for each of the three nanorings investigated – see Table S4.

Table S4. Details of the number of whole/intact or 'broken' rings observed for ***c*-P18b**, ***c*-P24b** and ***c*-P36b$_2$** following electrospray deposition on to a Au(111) substrate.

	***c*-P18b**	***c*-P24b**	***c*-P36b$_2$**
Whole rings	41	51	59
Broken rings	12	21	47
Proportion of whole rings	87%	71%	59%

S7 NMR, Mass, UV–vis–NIR Absorption and Fluorescence Spectra

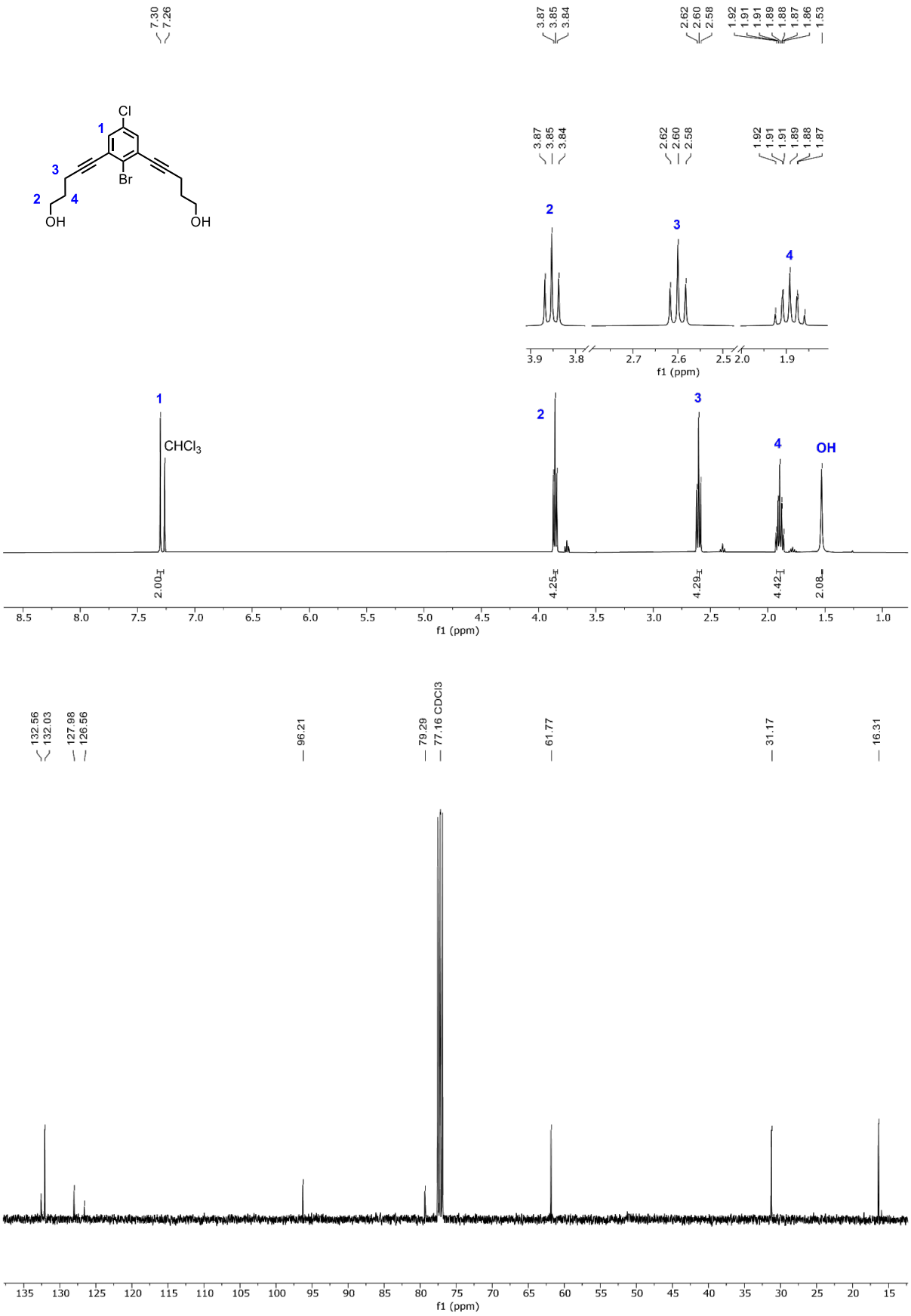

Figure S21. ^{1}H (400 MHz) and ^{13}C NMR (101 MHz) spectra for **S1** ($CDCl_3$, 298 K).

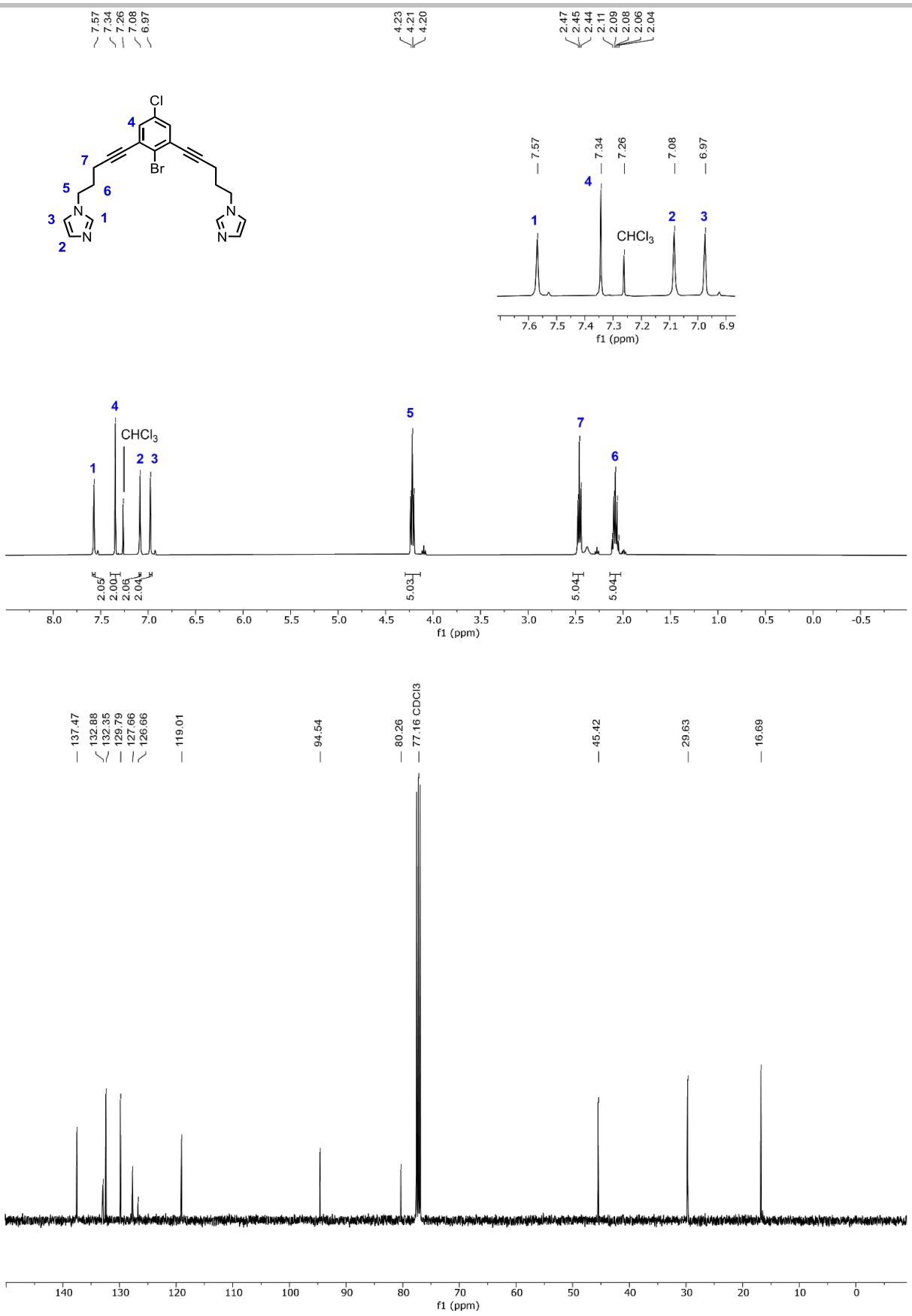

Figure S22. ^{1}H (400 MHz) and ^{13}C NMR (101 MHz) spectra for **S2** ($CDCl_3$, 298 K).

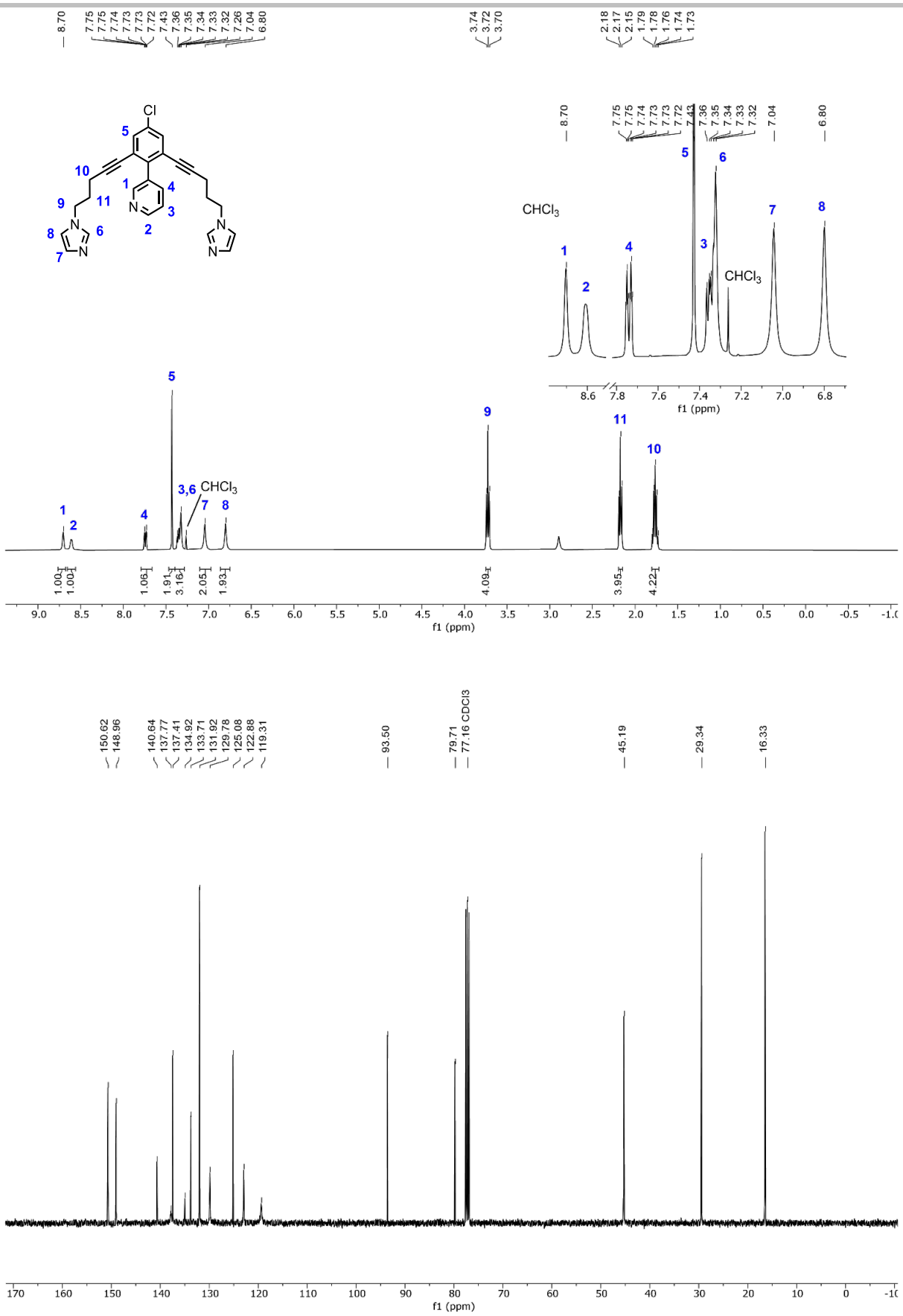

Figure S23. ^{1}H (400 MHz) and ^{13}C NMR (101 MHz) spectra for **T3** ($CDCl_3$, 298 K).

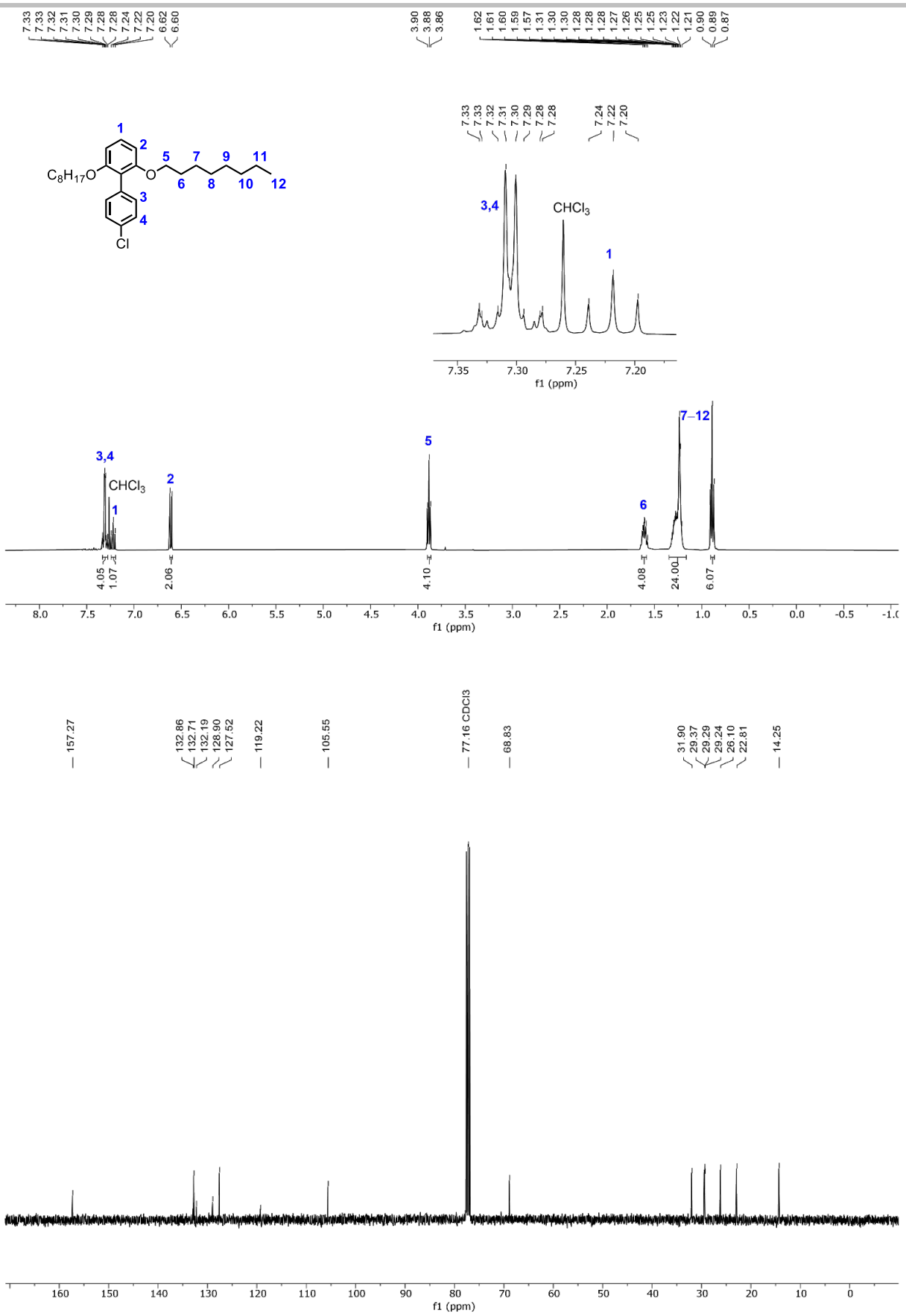

Figure S24. ^{1}H (400 MHz) and ^{13}C NMR (101 MHz) spectra for **S3** ($CDCl_3$, 298 K).

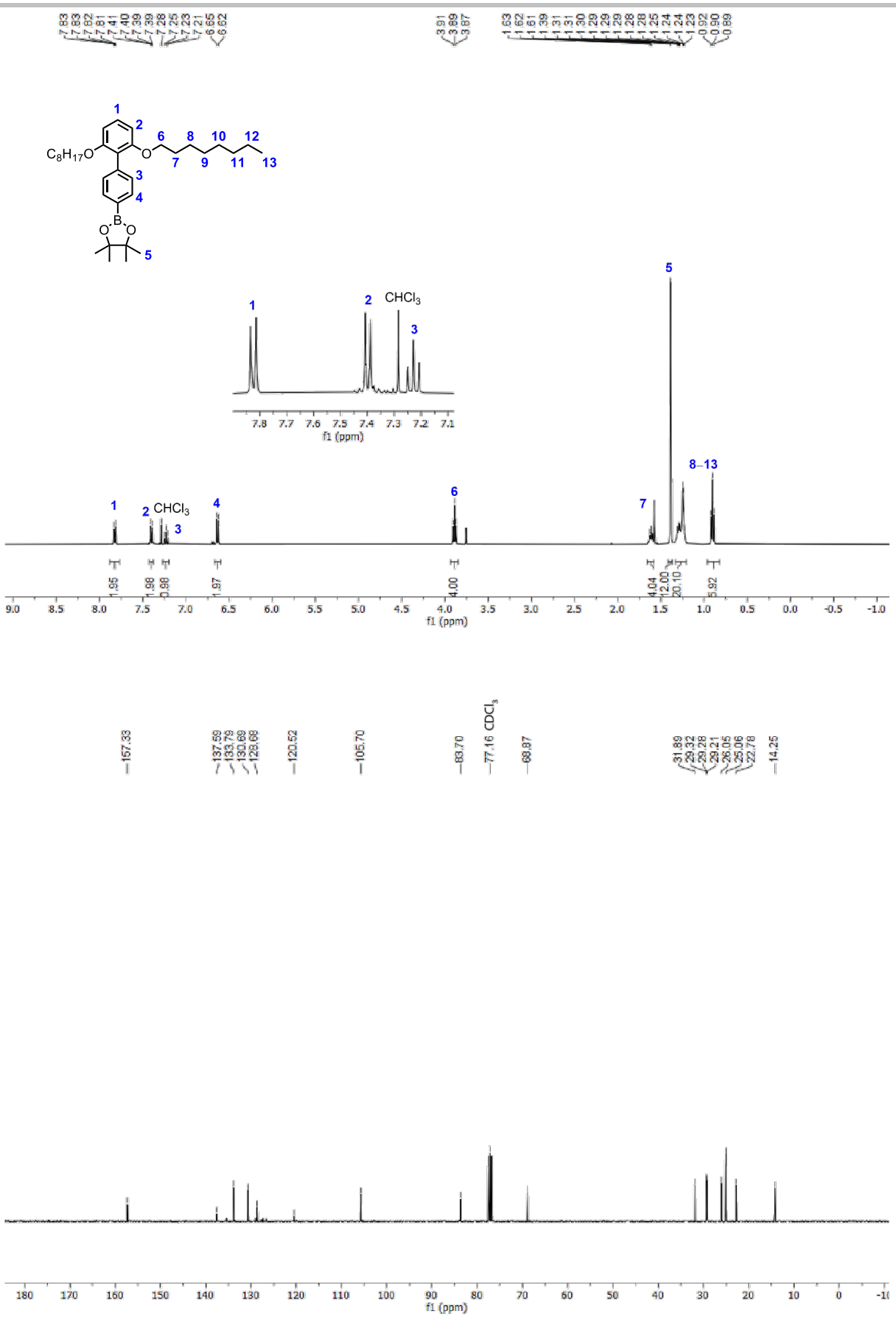

Figure S25. ^{1}H (400 MHz) and ^{13}C NMR (101 MHz) spectra for **S4** ($CDCl_3$, 298 K).

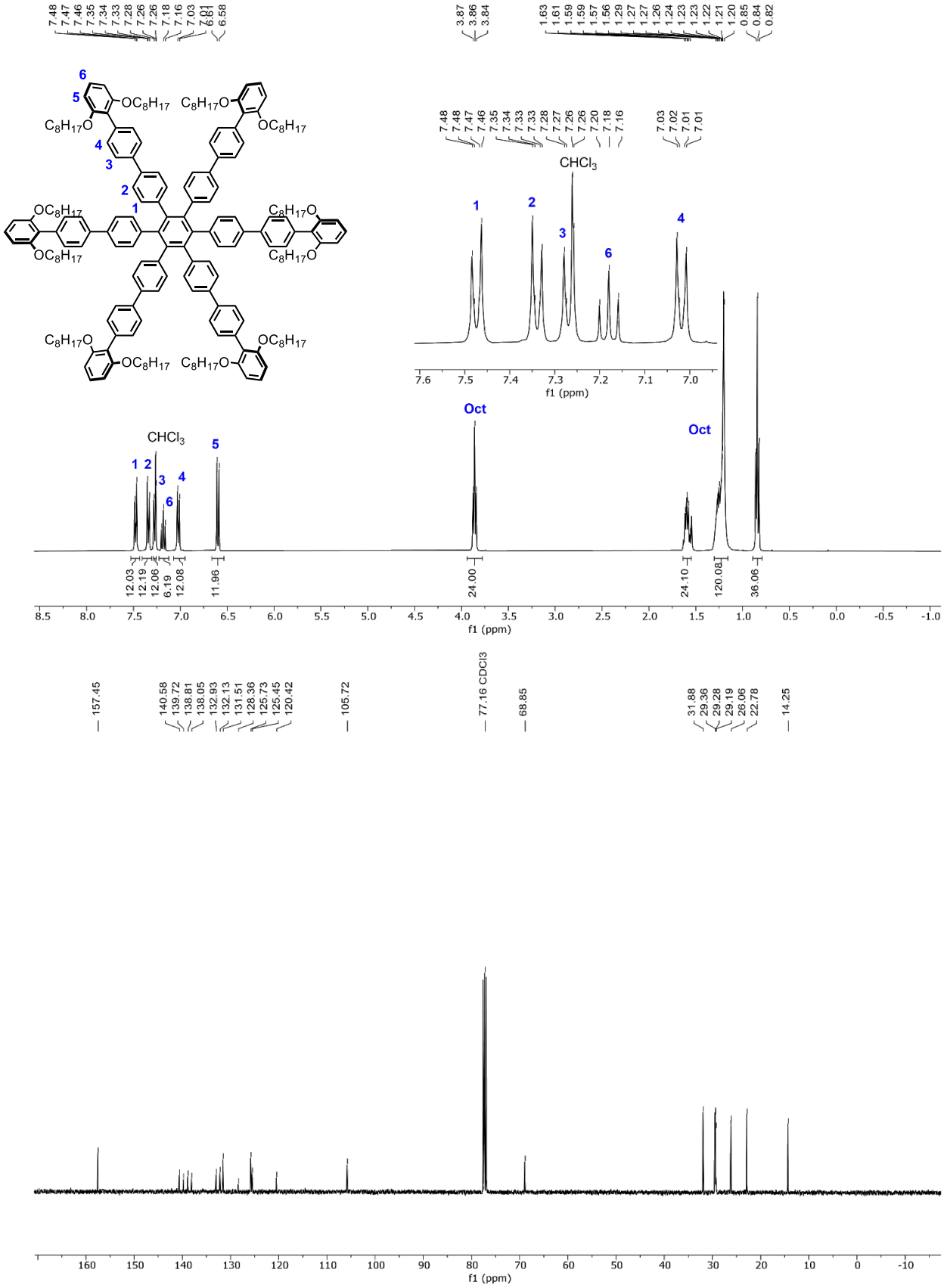

Figure S26. ^{1}H (400 MHz) and ^{13}C NMR (101 MHz) spectra for **S5** ($CDCl_3$, 298 K).

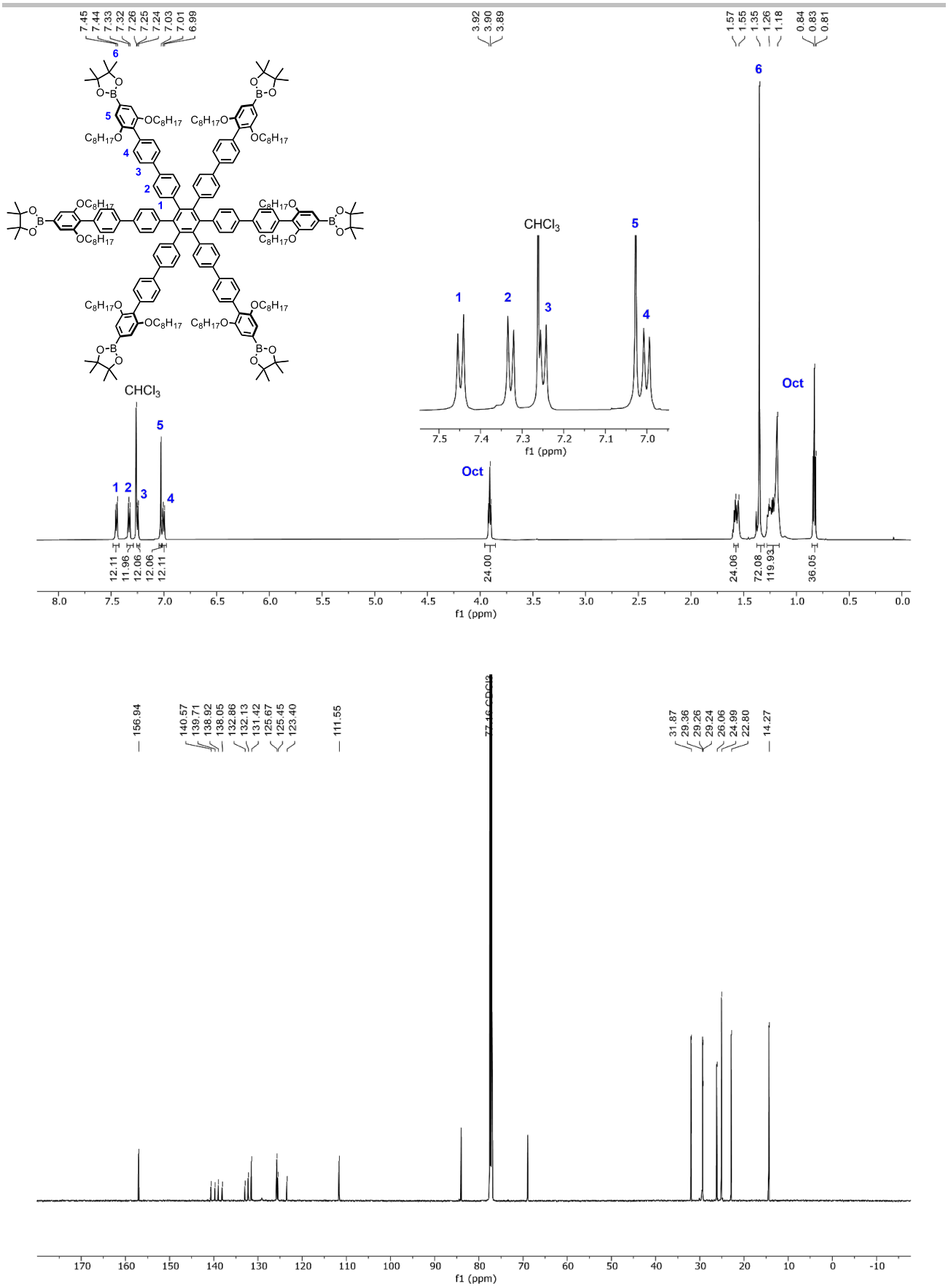

Figure S27. ^{1}H (600 MHz) and ^{13}C NMR (151 MHz) spectra for **S6** ($CDCl_3$, 298 K).

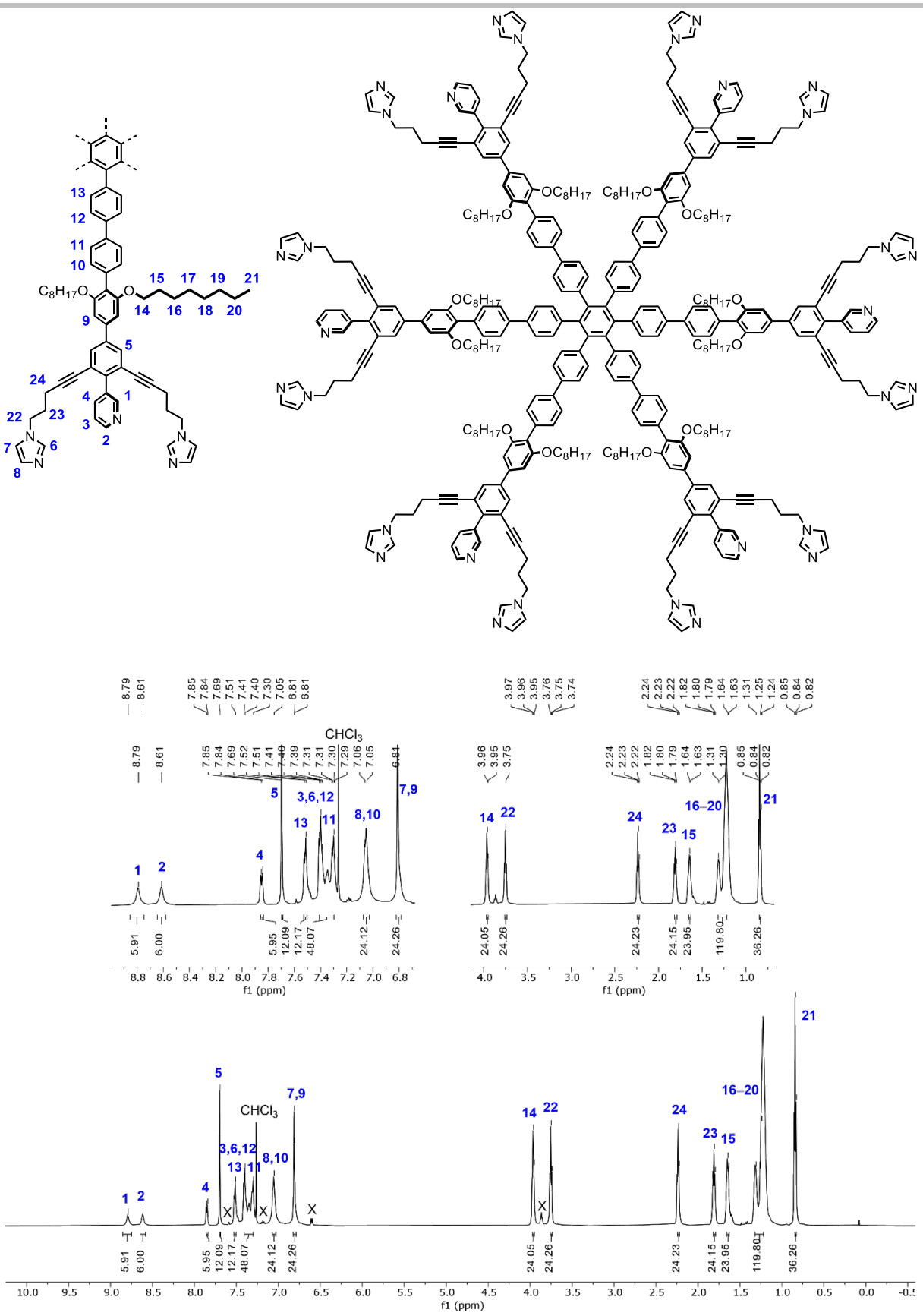

Figure S28. ^{1}H NMR spectrum for **T18** (600 MHz, $CDCl_3$, 298 K). X = Impurity.

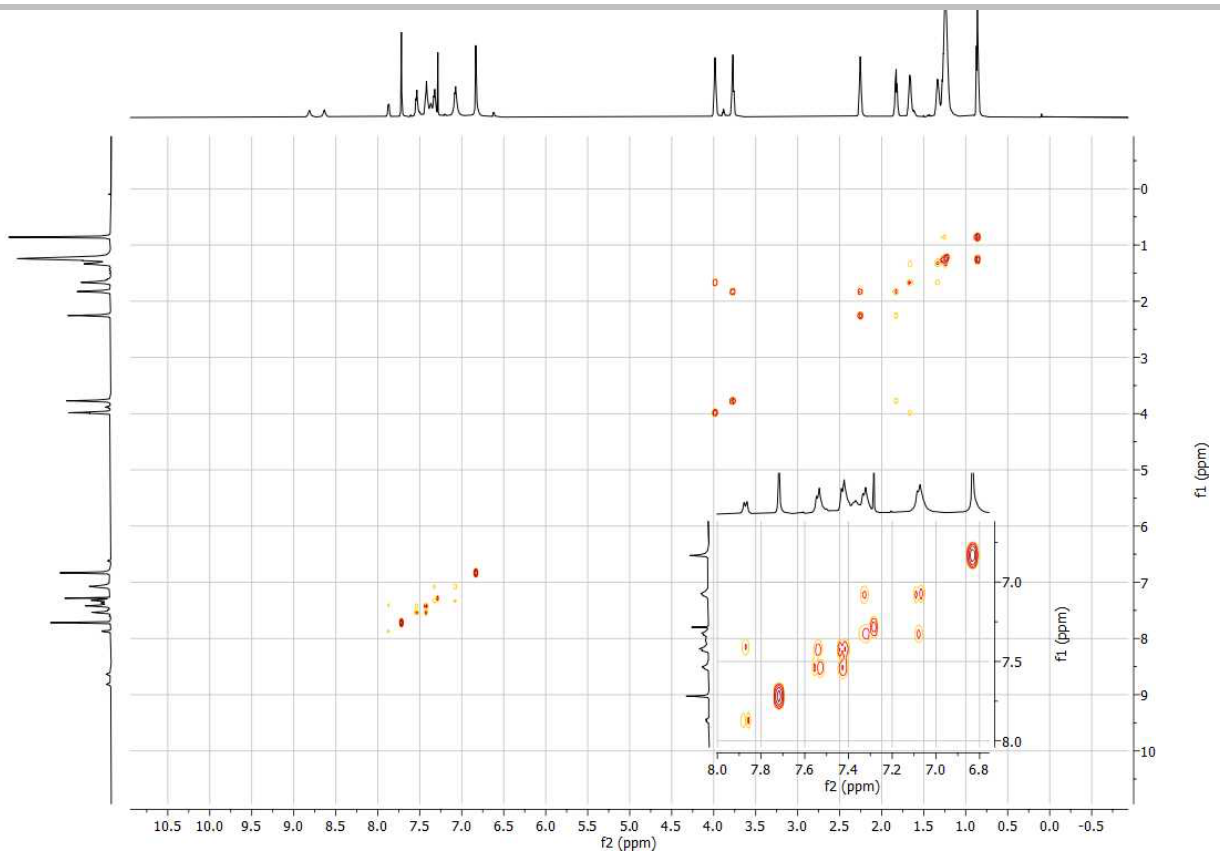

Figure S29. COSY spectrum for **T18** (600 MHz, $CDCl_3$, 298 K).

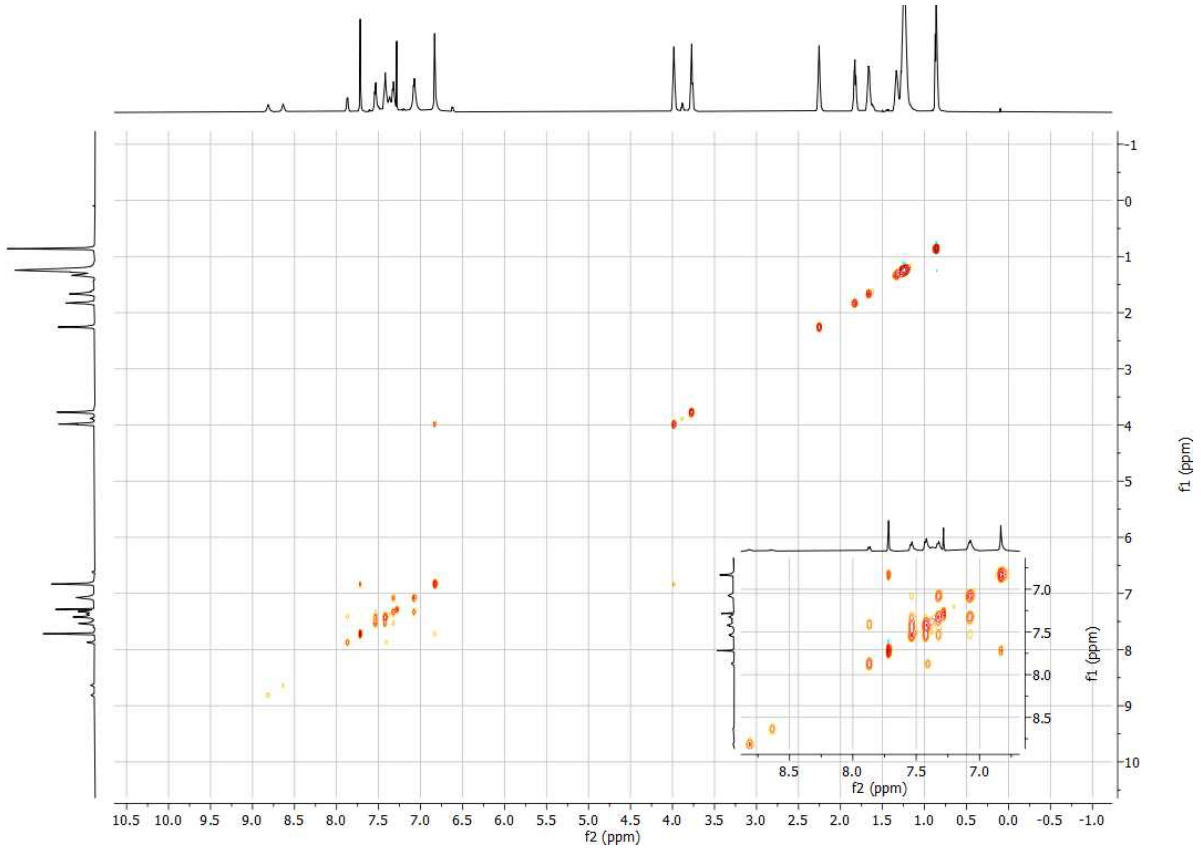

Figure S30. NOESY spectrum for **T18** (600 MHz, $CDCl_3$, 298 K).

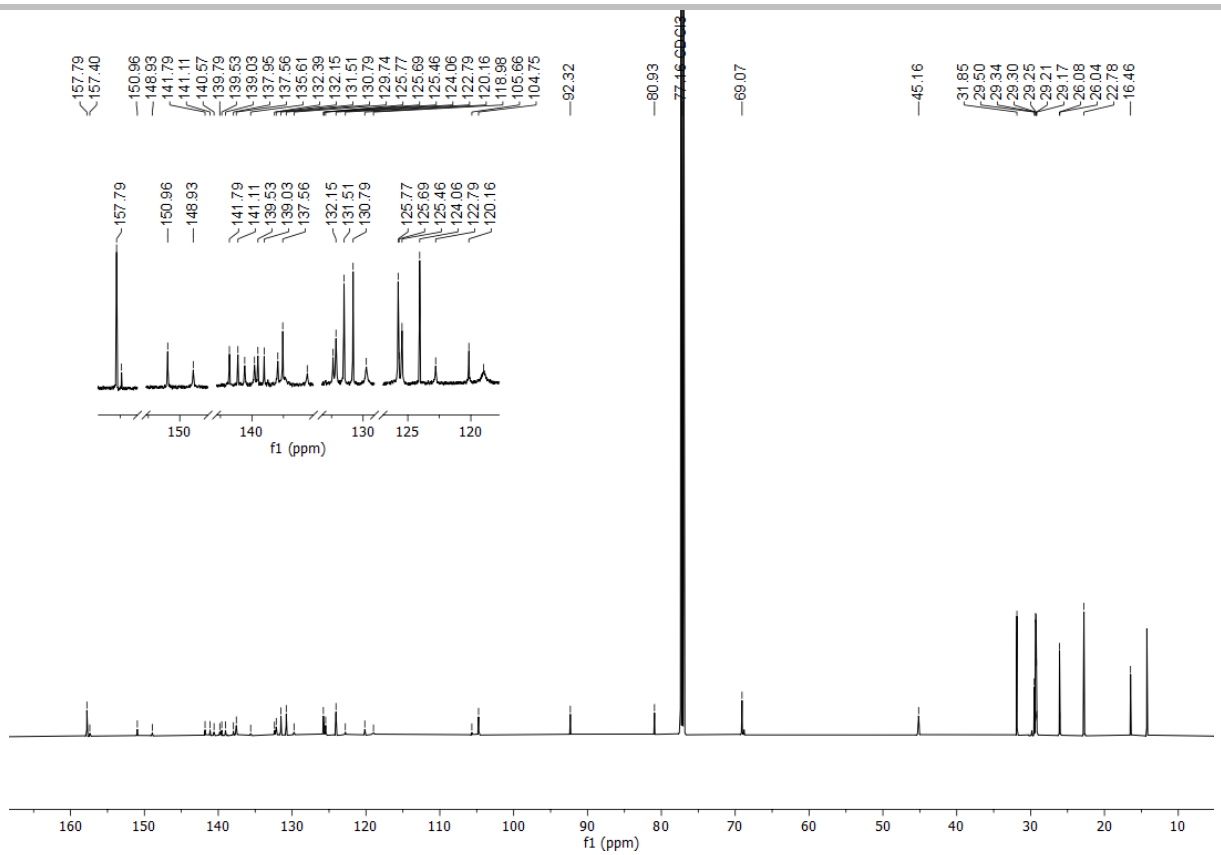

Figure S31. ^{13}C spectrum for **T18** (151 MHz, $CDCl_3$, 298 K).

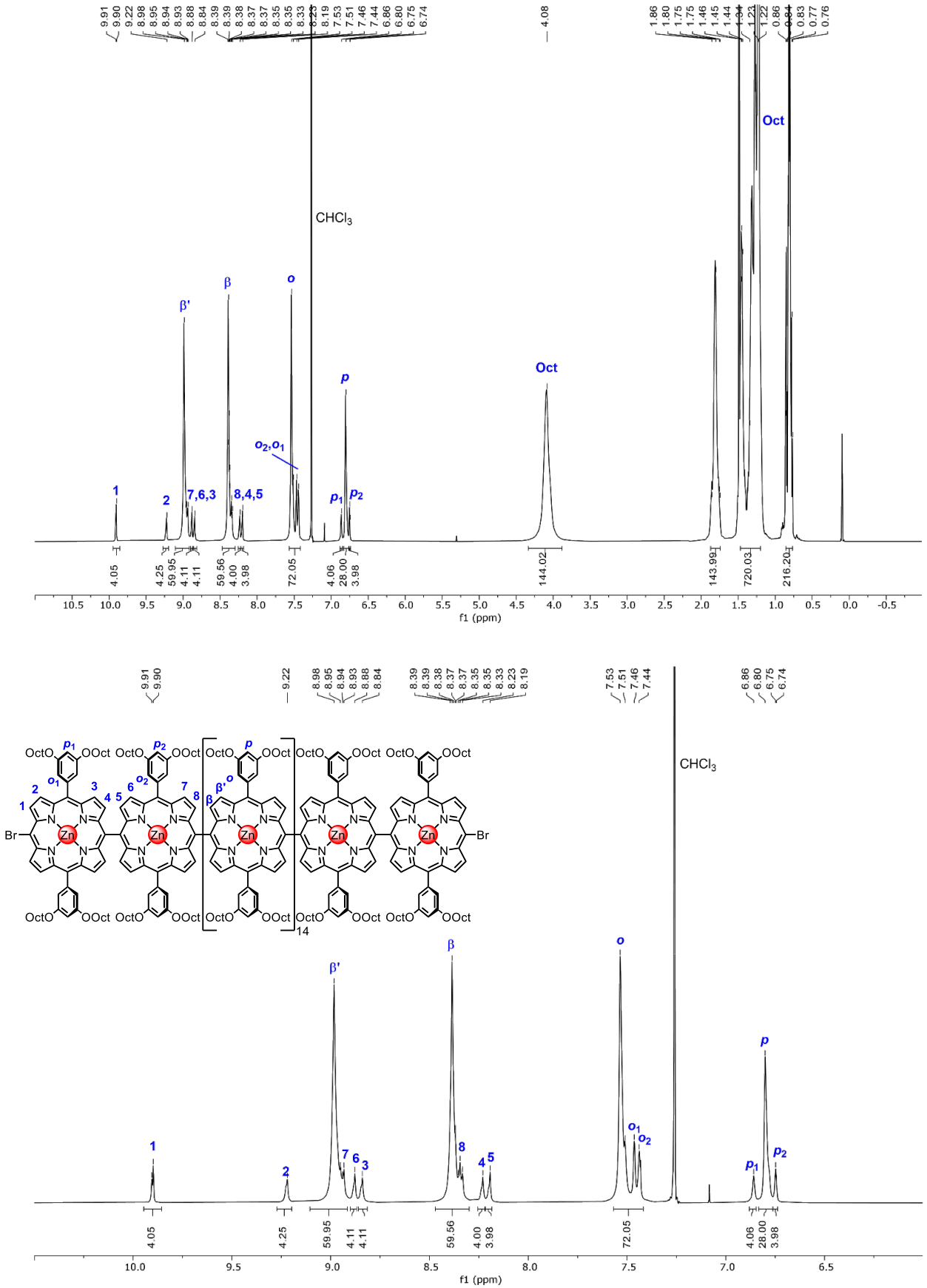

Figure S32. Full (top) and expanded (bottom) ^{1}H spectrum for ***ls*-P18-Br$_2$** (500 MHz, $CDCl_3$, 298 K).

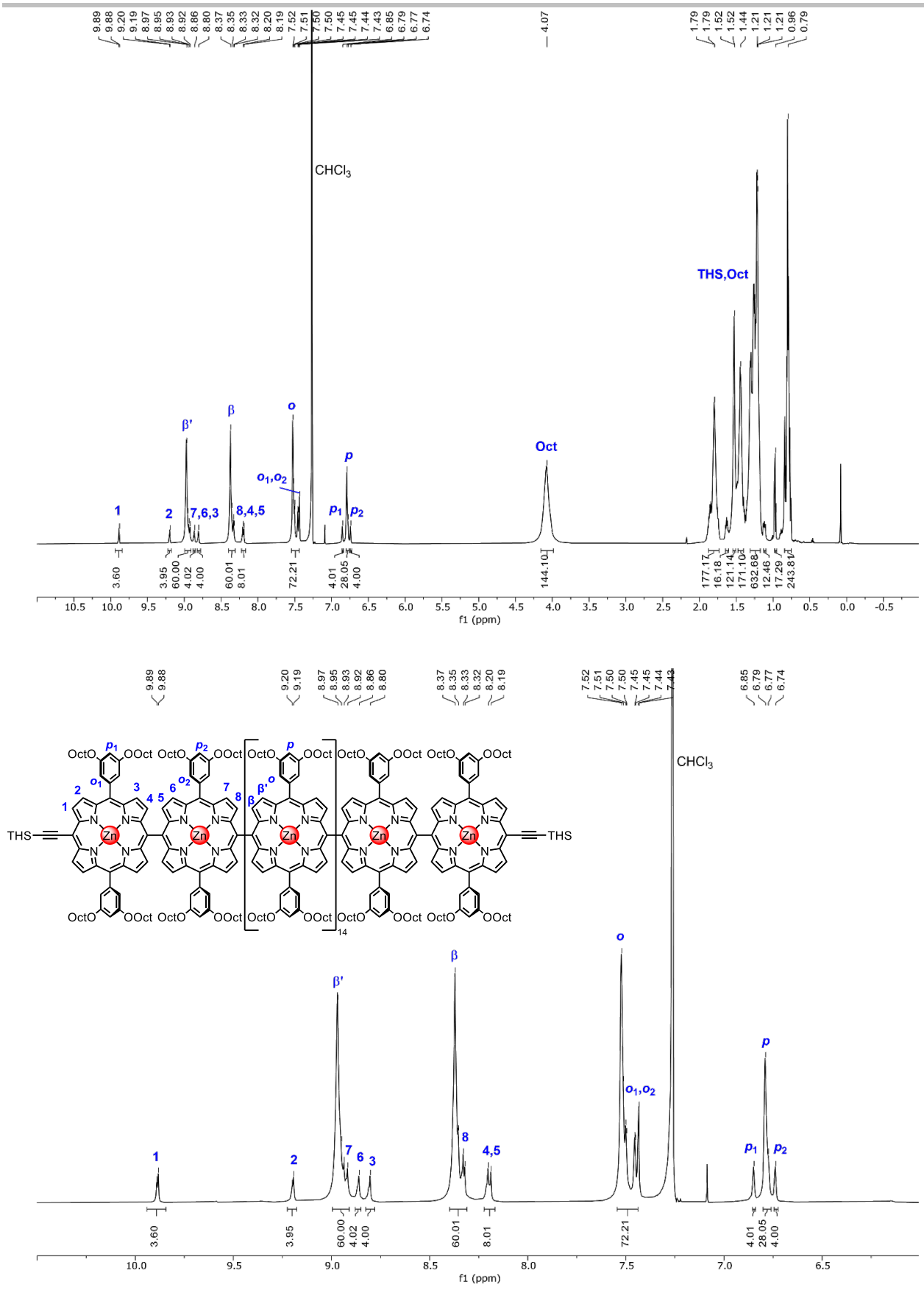

Figure S33. Full (top) and expanded (bottom) ^{1}H spectrum for ***ls*-P18-(C$_2$THS)$_2$** (500 MHz, $CDCl_3$, 298 K).

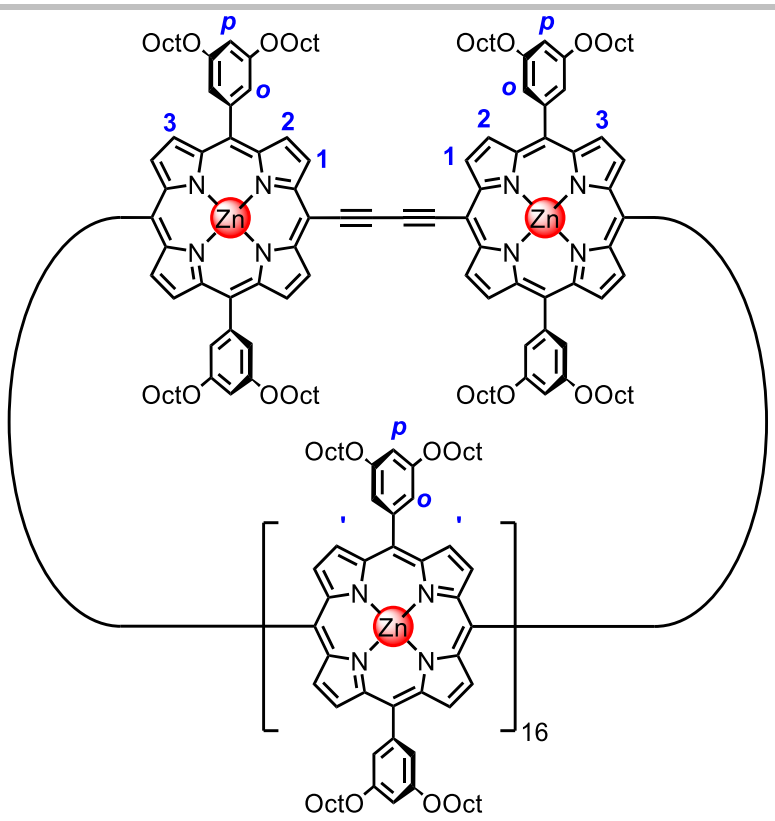

***c*-P18b**

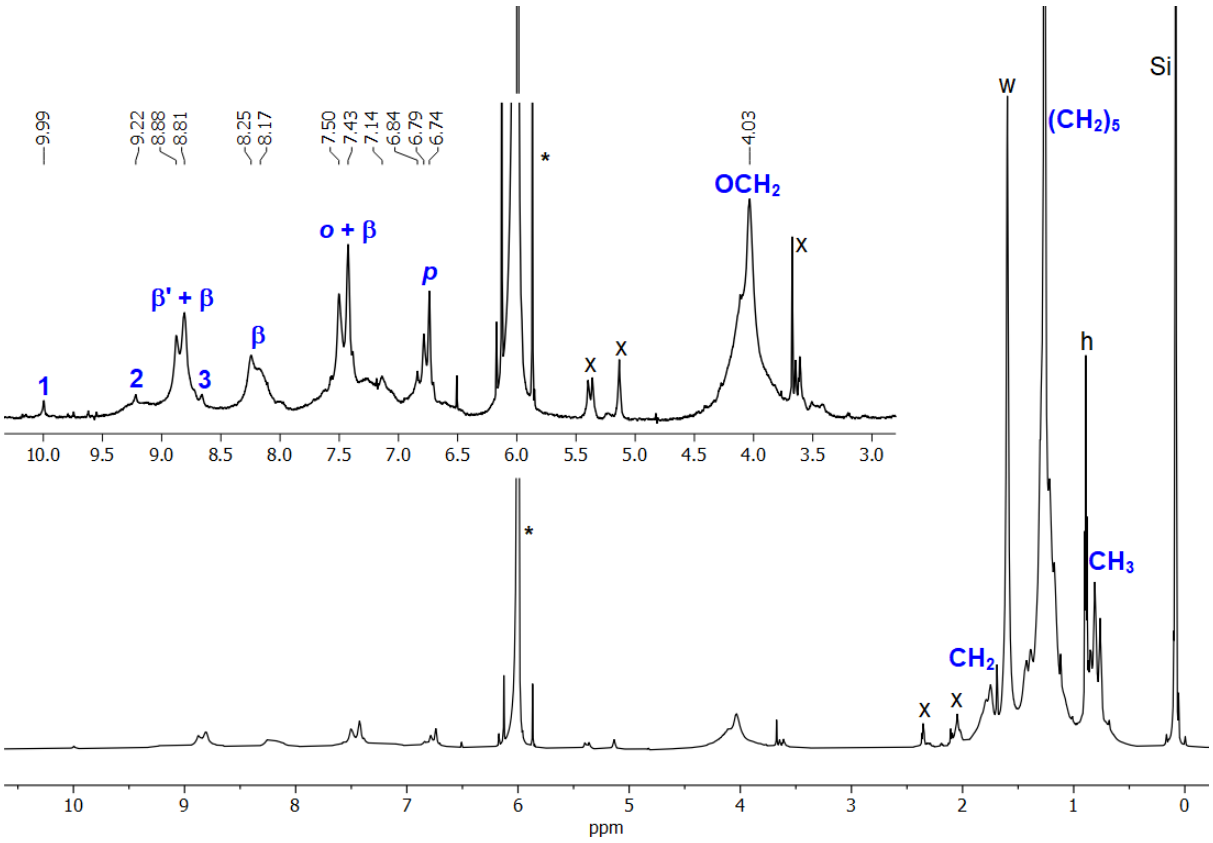

Figure S34. ^{1}H NMR spectrum of ***c*-P18b** (700 MHz, tetrachloroethane-d_2, 298 K). * = residual solvent signal; x = impurity; w = water; h = H-grease; Si = silicone grease.

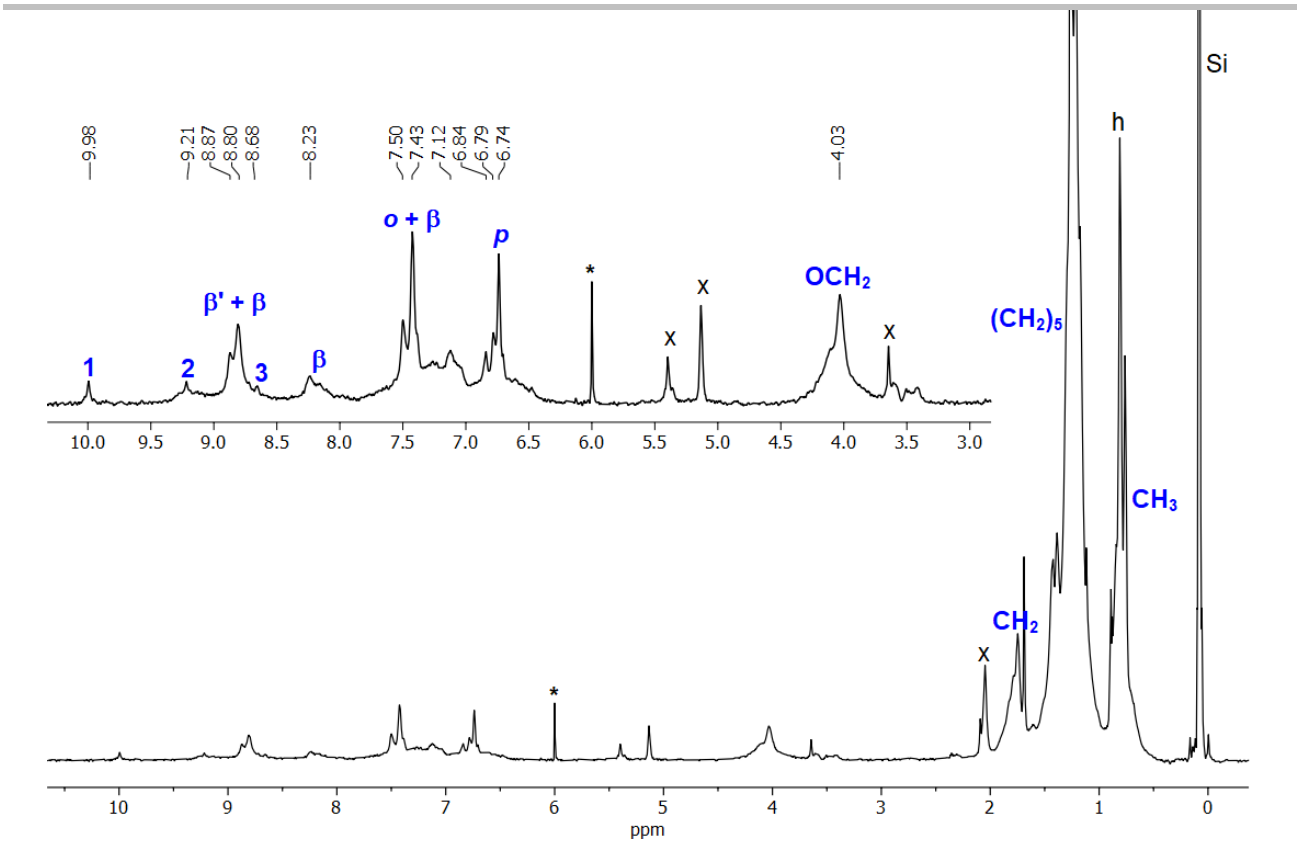

Figure S35. Diffusion-edited ^{1}H NMR spectrum of ***c*-P18b** (700 MHz, tetrachloroethane-d_2, 298 K). G = 42.8 G/cm, Δ = 0.1 s, and δ = 3000 µs. * = residual solvent signal; x = impurity; h = H-grease; Si = silicone grease.

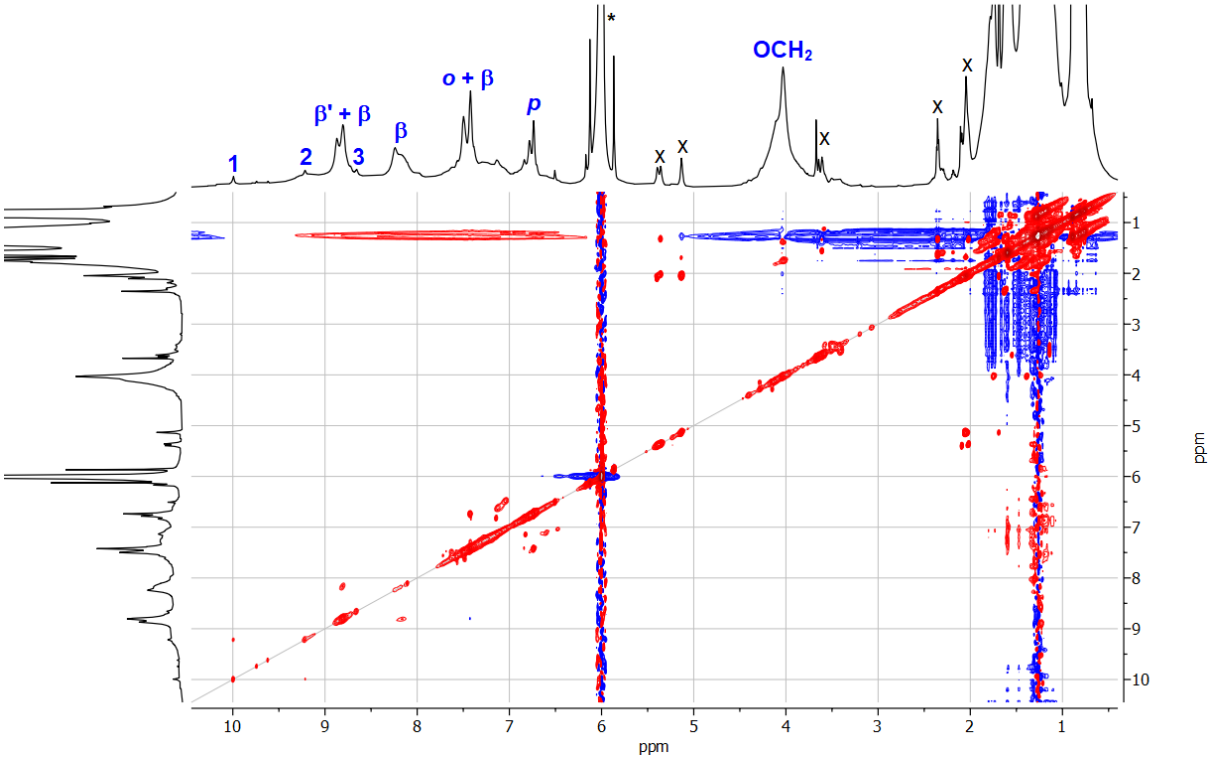

Figure S36. Full TOCSY spectrum (700 MHz, $CDCl_3$, 298 K) of ***c*-P18b**. Mixing time = 60 ms. * = residual solvent signal; x = impurity.

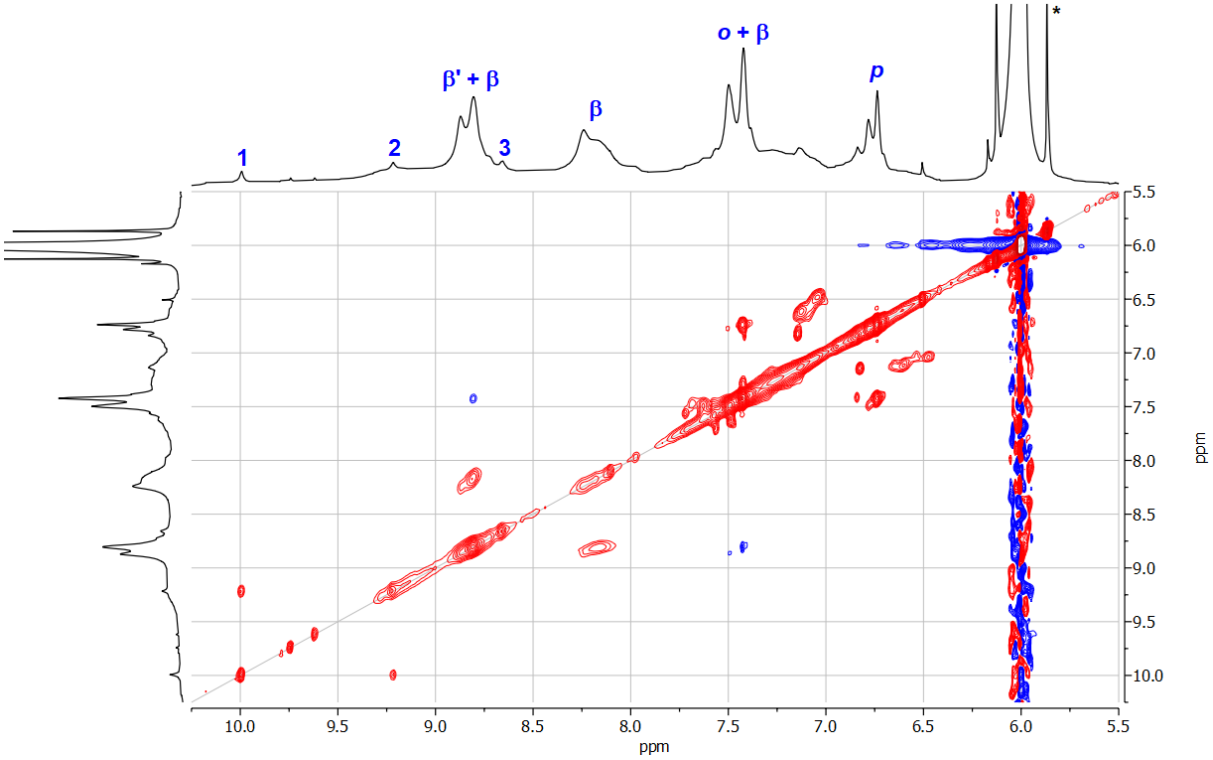

Figure S37. Ar-region of TOCSY spectrum (700 MHz, $CDCl_3$, 298 K) of ***c*-P18b**. Mixing time = 60 ms. * = residual solvent signal.

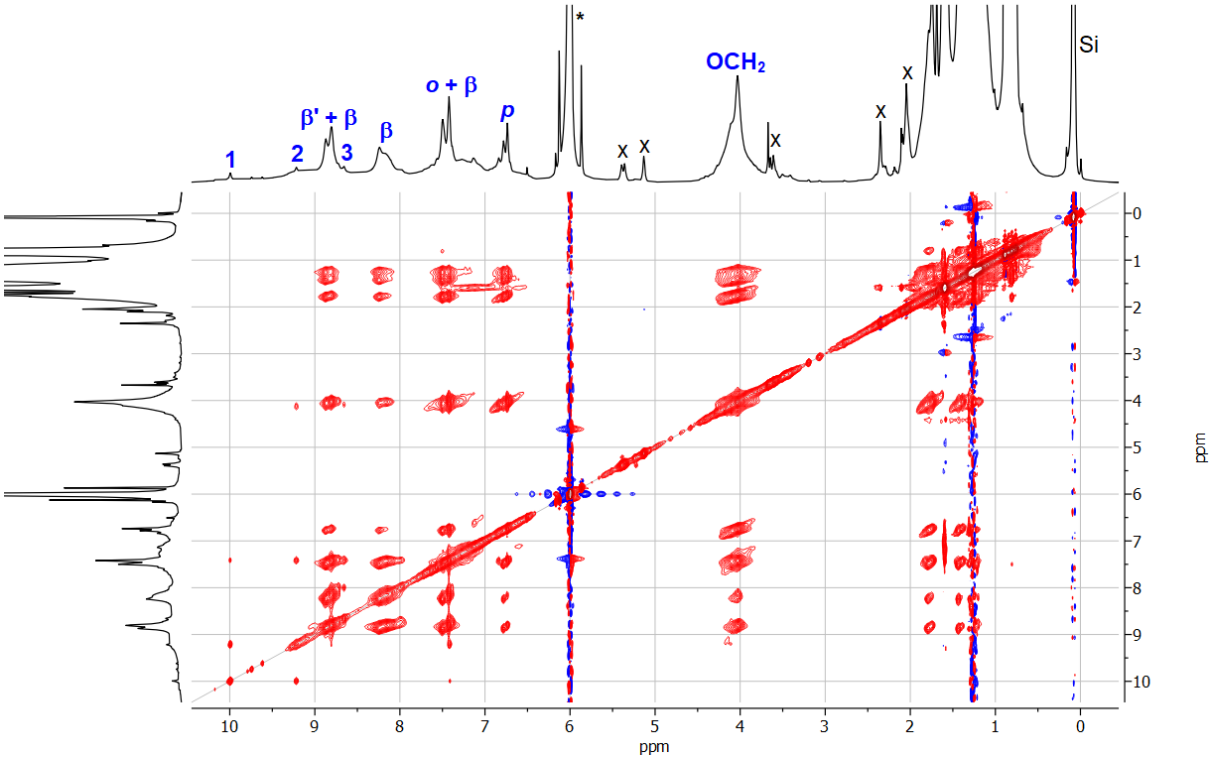

Figure S38. Full NOESY (700 MHz, $CDCl_3$, 298 K) spectrum of ***c*-P18b**. Mixing time = 400 ms. * = residual solvent signal; x = impurity; Si = silicone grease.

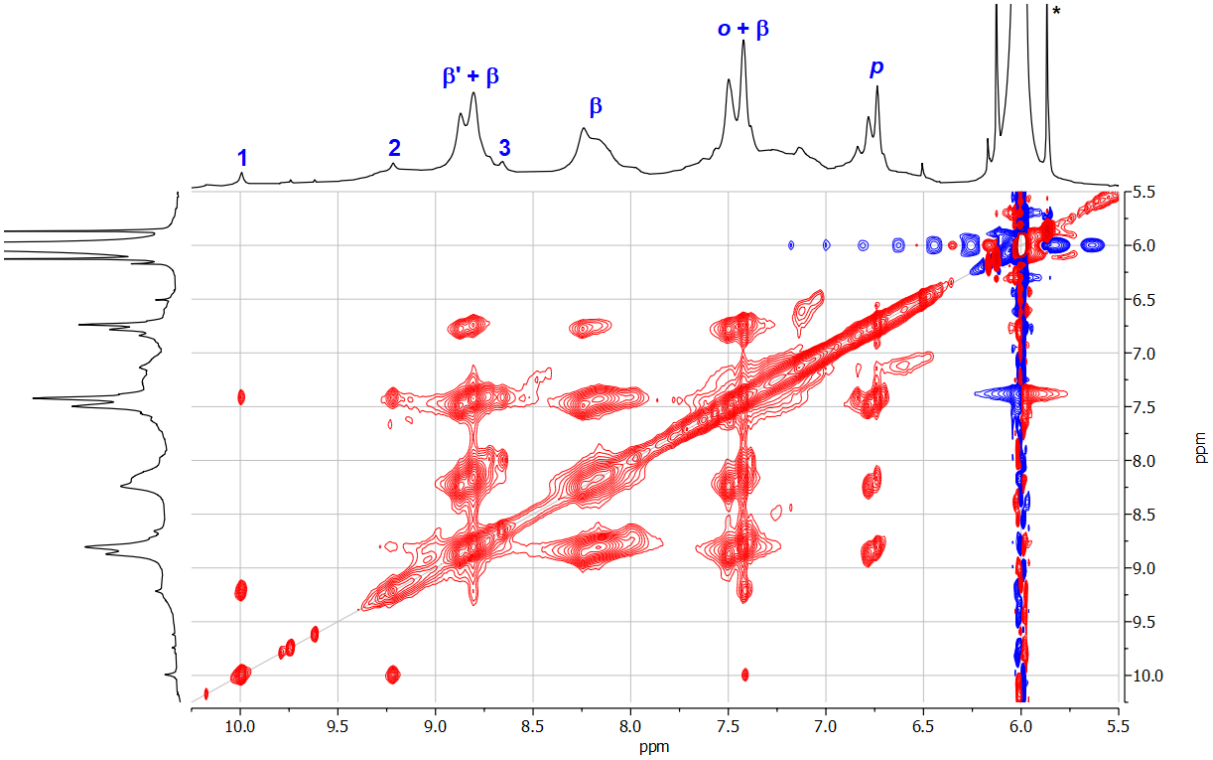

Figure S39. Ar-region of NOESY spectrum (700 MHz, $CDCl_3$, 298 K) of ***c*-P18b**. Mixing time = 400 ms. * = residual solvent signal.

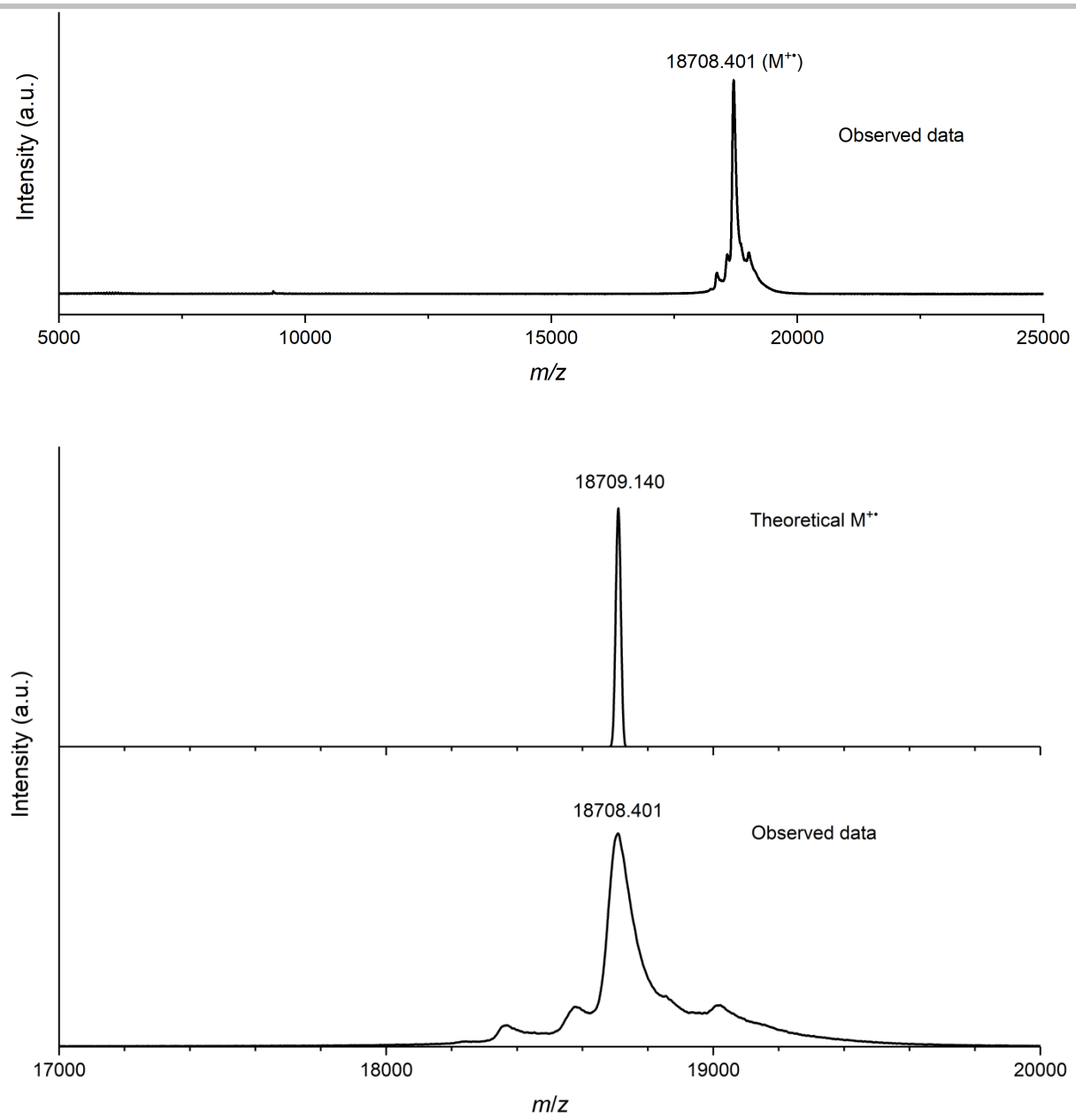

Figure S40. MALDI-ToF spectrum of ***c*-P18b** with DCTB as matrix. Overview (top) and zoomed-view of the $M^{+\bullet}$ region (bottom).

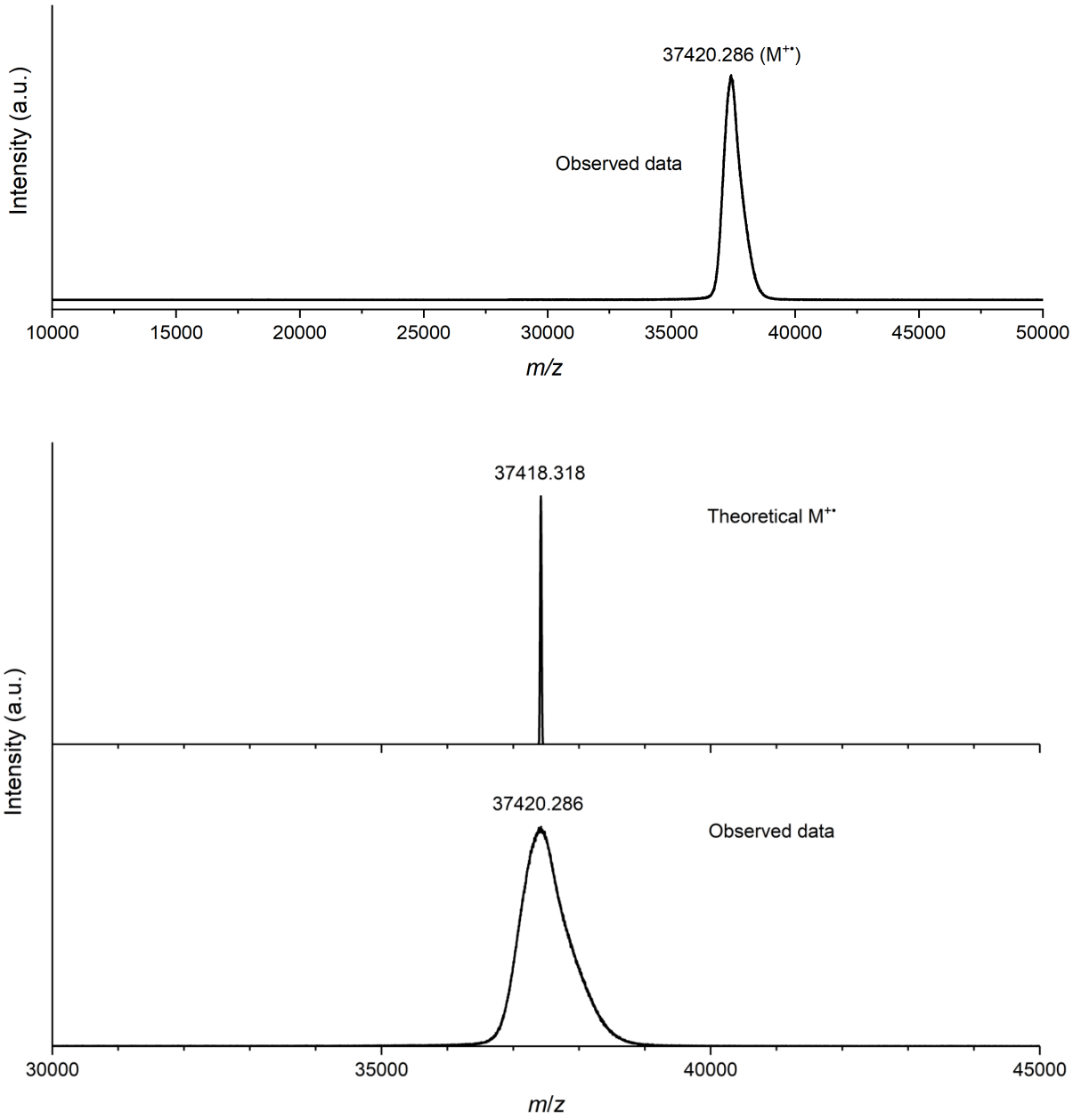

Figure S41. MALDI-ToF spectrum of ***c*-P36b$_2$** with DCTB as matrix. Overview (top) and zoomed-view of the M$^{+\bullet}$ region (bottom).

Absorption and Fluorescence Spectroscopy

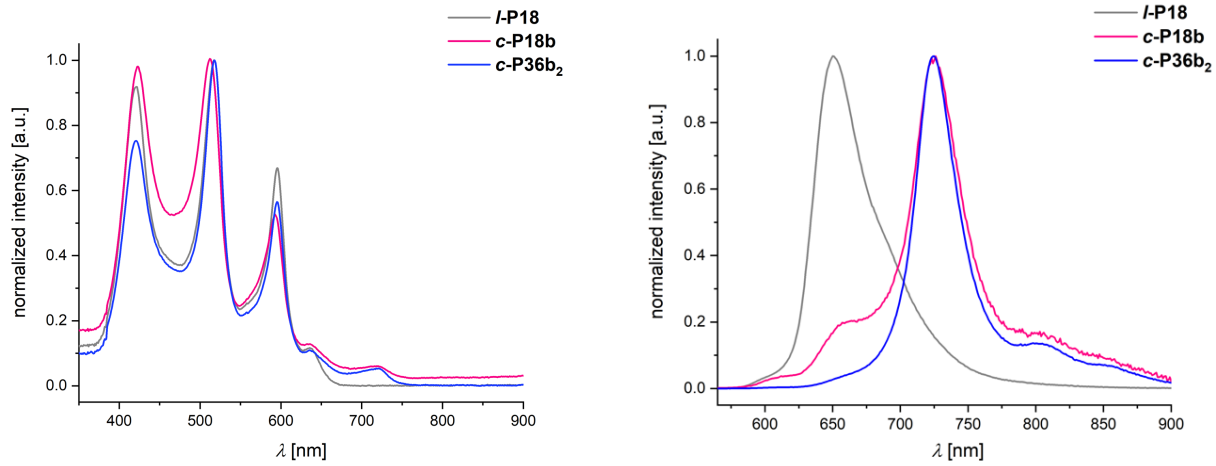

Figure S42. Normalized absorption spectra (left) and emission spectra (right) of ***l*-P18**, ***c*-P18b** and ***c*-P36b$_2$** (toluene + 1% pyridine, 298 K). The excitation wavelength for the fluorescence spectra is 550 nm.

S8 References

[1] R. Rathore, C. L. Burns, M. I. Deselnicu, *Org. Lett.* **2001**, *3*, 2887–2890.
[2] Y. Hirano, S. Kojima, Y. Yamamoto. *J. Org. Chem.* **2011**, *76*, 2123–2131.
[3] G. Marotta, Ch. P. Kumar, M. G. Lobello, F. Cavazzini, P. Salvatori, K. Ganesh, M. K. Nazeeruddin, M. Chandrasekharam, F. De Angelis, *Dalton Trans.* **2015**, *44*, 5369–5378.
[4] N. Aratani, A. Takagi, Y. Yanagawa, T. Matsumoto, T. Kawai, Z. S. Yoon, D. Kim, A. Osuka, *Chem. Eur. J.* **2005**, *11*, 3389–3404.
[5] H. Gotfredsen, J.-R. Deng, J. M. Van Raden, M. Righetto, J. Hergenhahn, M. Clarke, A. Bellamy-Carter, J. Hart, J. O'Shea, T. D. W. Claridge, F. Duarte, A. Saywell, L. M. Herz, H. L. Anderson, *Nat. Chem.* **2022**, *14*, 1436–1442.
[6] P. Thordarson, *Chem. Soc. Rev.* **2011**, *40*, 1305–1323.
[7] H. J. Hogben, J. K. Sprafke, M. Hoffmann, M. Pawlicki, H. L. Anderson, *J. Am. Chem. Soc.* **2011**, *133*, 20962–20969.
[8] M. J. Frisch, G. W. Trucks, H. B. Schlegel, G. E. Scuseria, M. A. Robb, J. R. Cheeseman, G. Scalmani, V. Barone, G. A. Petersson, H. Nakatsuji, X. Li, M. Caricato, A. V. Marenich, J. Bloino, B. G. Janesko, R. Gomperts, B. Mennucci, H. P. Hratchian, J. V. Ortiz, A. F. Izmaylov, J. L. Sonnenberg, D. WilliamsYoung, F. Ding, F. Lipparini, F. Egidi, J. Goings, B. Peng, A. Petrone, T. Henderson, D. Ranasinghe, V. G. Zakrzewski, J. Gao, N. Rega, G. Zheng, W. Liang, M. Hada, M. Ehara, K. Toyota, R. Fukuda, J. Hasegawa, M. Ishida, T. Nakajima, Y. Honda, O. Kitao, H. Nakai, T. Vreven, K. Throssell, J. A. Montgomery Jr., J. E. Peralta, F. Ogliaro, M. J. Bearpark, J. J. Heyd, E. N. Brothers, K. N. Kudin, V. N. Staroverov, T. A. Keith, R. Kobayashi, J. Normand, K. Raghavachari, A. P. Rendell, J. C. Burant, S. S. Iyengar, J. Tomasi, M. Cossi, J. M. Millam, M. Klene, C. Adamo, R. Cammi, J. W. Ochterski, R. L. Martin, K. Morokuma, O. Farkas, J. B. Foresman, D. J. Fox, Gaussian Inc. Wallingford CT, **2016**.
[9] C. Adamo, V. Barone, *J. Chem. Phys.* **1999**, *110*, 6158–6170.
[10] S. Grimme, S. Ehrlich, L. Goerigk, *J. Comp. Chem.* **2011**, *32*, 1456–1465.
[11] C. E. Colwell, T. W. Price, T. Stauch, R. Jasti, *Chem. Sci.* **2020**, *11*, 3923–3930.
[12] F. Neese, Wiley Interdisciplinary *Reviews: Computational Molecular Science* **2022**, 12, e1606.
[13] C. Bannwarth, S. Ehlert, S. Grimme, *J. Chem. Theory Comput.* **2019**, *15*, 1652–1671.
[14] D. A. Case, K. Belfon, I.Y. Ben-Shalom, S. R. Brozell, D. S. Cerutti, T. E. Cheatham, V. W. Cruzeiro, T. A. Darden, R. E. Duke, G. Giambasu, M. K. Gilson, H. Gohlke, A. W. Goetz, R. Harris, S. Izadi, S. A. Izmailov, K. Kasavajhala, A. Kovalenko, R. Krasny, T. Kurtzman, T. S. Lee, S. LeGrand, P. Li, C. Lin, J. Liu, T. Luchko, R. Luo, V. Man, K. M. Merz, Y. Miao, O. Mikhailovskii, G. Monard, H. Nguyen, A. Onufriev, F. Pan, S. Pantano, R. Qi, D. R. Roe, A. Roitberg, C. Sagui, S. Schott-Verdugo, J. Shen C. L. Simmerling, N. R. Skrynnikov, J. Smith, J. Swails, R. C. Walker, J. Wang, L. Wilson, R. M. Wolf, X. Wu, Y. Xiong, Y. Xue, D. M. York P. A. Kollman, AMBER 2020, University of California, San Francisco.
[15] J. M. Wang, R. M. Wolf, J. W. Caldwell, P. A. Kollman, D. A. Case, *J. Comput. Chem.* **2004**, *25*, 1157–1174.
[16] M. J. Abraham, T. Murtola, R. Schulz, S. Páll, J. C. Smith, B. Hess, E. Lindahl, *SoftwareX* **2015**, *1–2*, 19–25.
[17] G. Bussi, D. Donadio, M. Parrinello, *J. Chem. Phys.* **2007**, *126*, 014101.
[18] M. Parrinello, A. Rahman, *J. Appl. Phys.* **1981**, *52*, 7182–7190.
[19] P. Cieplak, J. Caldwell, P. Kollman, *J. Comput. Chem.* **2001**, *22*, 1048–1057.
[20] U. Essmann, L. Perera, M. L. Berkowitz, T. Darden, H. Lee, L. G. Pedersen, *J. Chem. Phys.* **1995**, *103*, 8577–8593.
[21] B. Hess, H. Bekker, H.J.C. Berendsen, J.G.E.M. Fraaije, *J. Comp. Chem.* **1997**, *18*, 1463–1472.

Author Contributions

J.M.V.R., J.-R.D., H.G., J. Hergenhahn and H.L.A. designed the **T18** template and conceived the project. J. Hergenhahn carried out the computational modelling, with support from F.D., after preliminary modelling by H.G., J.-R.D. and J.M.V.R. The synthesis and chemical characterization was performed by J.M.V.R., J.-R.D. and H.G. Scanning probe microscopy was performed by M.C., M.E. and A.S., after J. Hart and J.N.O. prepared samples via electrospray deposition. J.M.V.R., J.-R.D., H.G., J. Hergenhahn and H.L.A. wrote the paper; all authors discussed the results and edited the manuscript.